Article

BCL7A-containing SWI/SNF/BAF complexes modulate mitochondrial bioenergetics during neural progenitor differentiation

Lena Wischhof[1] , Hang-Mao Lee[1] , Janine Tutas[1] , Clemens Overkott[1], Eileen Tedt[1], Miriam Stork[1], Michael Peitz[2,3] , Oliver Brüstle[2] , Thomas Ulas[4], Kristian Händler[4], Joachim L Schultze[4,5], Dan Ehninger[1], Pierluigi Nicotera[1] , Paolo Salomoni[1] & Daniele Bano[1,*]

Abstract

Mammalian SWI/SNF/BAF chromatin remodeling complexes influence cell lineage determination. While the contribution of these complexes to neural progenitor cell (NPC) proliferation and differentiation has been reported, little is known about the transcriptional profiles that determine neurogenesis or gliogenesis. Here, we report that BCL7A is a modulator of the SWI/SNF/BAF complex that stimulates the genome-wide occupancy of the ATPase subunit BRG1. We demonstrate that BCL7A is dispensable for SWI/SNF/BAF complex integrity, whereas it is essential to regulate Notch/Wnt pathway signaling and mitochondrial bioenergetics in differentiating NPCs. Pharmacological stimulation of Wnt signaling restores mitochondrial respiration and attenuates the defective neurogenic patterns observed in NPCs lacking BCL7A. Consistently, treatment with an enhancer of mitochondrial biogenesis, pioglitazone, partially restores mitochondrial respiration and stimulates neuronal differentiation of BCL7A-deficient NPCs. Using conditional BCL7A knockout mice, we reveal that BCL7A expression in NPCs and postmitotic neurons is required for neuronal plasticity and supports behavioral and cognitive performance. Together, our findings define the specific contribution of BCL7A-containing SWI/SNF/BAF complexes to mitochondria-driven NPC commitment, thereby providing a better understanding of the cell-intrinsic transcriptional processes that connect metabolism, neuronal morphogenesis, and cognitive flexibility.

Introduction

Adult neural stem cells (NSCs) are found in the adult mouse brain, mostly restricted to the subgranular zone (SGZ) of the hippocampal dentate gyrus and the subventricular zone (SVZ) of the lateral ventricles (Bond *et al*, 2015; Kempermann, 2015; Kempermann *et al*, 2015, 2018; Goncalves *et al*, 2016; Gotz *et al*, 2016; Lim & Alvarez-Buylla, 2016; Falk & Gotz, 2017; Obernier & Alvarez-Buylla, 2019; Toda *et al*, 2019). In response to environmental cues, transient-amplifying (or intermediate) progenitors have the potential to differentiate into mature neurons that can functionally integrate into the existing neural network, thereby contributing to brain plasticity and cognitive functions (Erickson *et al*, 2011; Kempermann *et al*, 2018; Toda *et al*, 2019). Alternatively, adult neural progenitor cells (NPCs) can progressively become glial cells, in part because of the predominant gliogenic properties of the surrounding milieu (Goncalves *et al*, 2016; Gotz *et al*, 2016; Falk & Gotz, 2017). A large literature has highlighted a complex crosstalk between regulatory mechanisms controlling NSC fate during neurodevelopment as well as in adult organisms (Bond *et al*, 2015; Goncalves *et al*, 2016; Silbereis *et al*, 2016; Yao *et al*, 2016). Although experimental and clinical evidence has indicated a key contribution of chromatin remodeling in this decision-making process (Son & Crabtree, 2014; Goncalves *et al*, 2016; Yao *et al*, 2016; Sokpor *et al*, 2017; Kempermann *et al*, 2018), the transcriptional profiles that define NSC differentiation toward neurons or glia remain poorly characterized.

Switch/sucrose nonfermentable (SWI/SNF) complex belongs to the large family of ATP-dependent chromatin remodelers. In higher organisms, SWI/SNF/BAF complexes contribute to the regulation of the transcriptional machinery at targeted genomic regions through the dynamic control of nucleosomal DNA (Schuettengruber *et al*, 2017; Sartorelli & Puri, 2018; Mittal & Roberts, 2020). The two mutually exclusive ATPases, namely SMARCA2/BRM and SMARCA4/BRG1, assemble with a collection of dedicated core

1 German Center for Neurodegenerative Diseases (DZNE), Bonn, Germany
2 Institute of Reconstructive Neurobiology, University of Bonn Medical Faculty and University Hospital Bonn, Bonn, Germany
3 Cell Programming Core Facility, University of Bonn Medical Faculty, Bonn, Germany
4 PRECISE Platform for Single Cell Genomics and Epigenomics, German Center for Neurodegenerative Diseases (DZNE) and the University of Bonn, Bonn, Germany
5 Department for Genomics and Immunoregulation, LIMES Institute, University of Bonn, Bonn, Germany
*Corresponding author. Tel: +0049 228 43302 510; Fax: +0049 228 43302 689; E-mail: daniele.bano@dzne.de

subunits and associated factors that critically influence the stability, structure, and functionality of individual SWI/SNF complexes (Kadoch et al, 2013; Schick et al, 2019). The combinatorial assembly of one ATPase with a set of BRG1/BRM-associated factors (BAFs) can generate many different macromolecular complexes with a molecular weight of approximately 1.0–1.5 MDa. The core of structural subunits (i.e., SMARCD1-2-3/BAF60A-B-C, SMARCC1/BAF155) acts as a scaffolding platform for the incorporation of components (e.g., ARID1/BAF250, ARID2/BAF200, and GLTSCR1/BICRA) that direct the assembly of the nascent remodelers toward canonical BAF (cBAF), polybromo-associated BAF (PBAF), and noncanonical BAF (ncBAF/GBAF; Mashtalir et al, 2018; Michel et al, 2018; Valencia & Kadoch, 2019). The recruitment of the ATPase module, consisting of BRM/BRG1, SS18/L1, β-actin, ACTL6A/B, and one of the nonexchangeable BCL7A/B/C subunits, is the last common step that finalizes the biogenesis of these nonredundant forms of the SWI/SNF/BAF complex (Mashtalir et al, 2018, 2020). During metazoan evolution, the SWI/SNF/BAF complex has acquired novel features that have broadened the participation to countless biological processes. According to the current literature (Helming et al, 2014; Romero & Sanchez-Cespedes, 2014; Son & Crabtree, 2014; Choi et al, 2015; Kadoch & Crabtree, 2015; Kadoch et al, 2016; Schuettengruber et al, 2017; Sokpor et al, 2017; Sartorelli & Puri, 2018; Alfert et al, 2019; Bracken et al, 2019), the functional versatility of SWI/SNF/BAF complexes is mechanistically linked to the incorporation and/or exchange of distinct components capable of interacting with a certain spectrum of modifiers, corepressors and/or co-activators. The subsequent genome targeting of certain SWI/SNF/BAF assemblies enables the correct integration of intra- and extracellular signals into transcriptional profiles that delineate cell fate.

Substantial clinical and experimental evidence indicates that alterations of the SWI/SNF/BAF complex may cause human diseases (Romero & Sanchez-Cespedes, 2014; Kadoch et al, 2016; Alfert et al, 2019; Bracken et al, 2019; Mittal & Roberts, 2020). Apart from the well-described causality in tumorigenesis (Kadoch et al, 2013; Shain & Pollack, 2013; Helming et al, 2014; Hohmann & Vakoc, 2014; Bracken et al, 2019), aberrant SWI/SNF/BAF complex activity has also been implicated in rare genetic forms of neurodevelopmental syndromes (Ronan et al, 2013; Son & Crabtree, 2014; Choi et al, 2015; Alfert et al, 2019). In this respect, a number of studies has described the SWI/SNF/BAF complex in the regulation of stem cell fate as well as neural lineage determination and differentiation. In the case of pathogenic alleles linked to Coffin-Siris syndrome, heterozygous single-residue mutations in the SMARCB1/BAF47 gene cause partial inhibition of SWI/SNF/BAF complex-mediated nucleosome binding and remodeling, whereby the aberrant expression of essential genes disrupt stem cell maintenance and neurogenesis (Tsurusaki et al, 2012, 2014; Valencia et al, 2019). As an additional case point, the exchange of dedicated SWI/SNF/BAF complex subunits has been shown to establish transcriptional profiles that timely dictate the switch from neural stem cells (NSCs) undergoing self-renewal and/or proliferation to neural progenitor cells (NPCs) committed to a neuronal fate. In particular, this is the case of BAF53A and BAF53B, with the former being indispensable for stemness and pluripotency, whereas the latter replacing BAF53A in the SWI/SNF/BAF complex to induce neuronal differentiation upon NPC commitment (Lessard et al, 2007; Wu et al, 2007; Vogel-Ciernia et al, 2013; Yoo et al, 2017; Zhu et al, 2017). Together, these studies emphasize the engagement of different SWI/SNF/BAF complexes in neurogenesis during embryonic development and possibly at adulthood.

To better understand the contribution of distinct SWI/SNF/BAF complexes in neurogenesis, we set out to profile the expression of SWI/SNF/BAF complex subunits during the differentiation of mouse-derived embryonic stem cells and human induced-pluripotent stem cells (iPSCs) toward NPCs and neurons. We describe that the B-cell lymphoma/leukemia protein 7A (BCL7A; Zani et al, 1996; Wischhof et al, 2017), a dedicated nonexchangeable subunit of the ATPase module (Kadoch et al, 2013; Mashtalir et al, 2018, 2020), is a critical regulator of neuronal differentiation in vitro as well as in vivo. Here, we report the mechanistic imprinting of the SWI/SNF/BAF complex in NPC lineage choice and differentiation, which depends on the transcriptional regulation of genes that potentiate mitochondrial OXPHOS.

Results

BCL7A is upregulated in NPCs and neurons

It has been suggested that the incorporation and/or replacement of distinct SWI/SNF/BAF complex components can influence neural lineage determination and differentiation (Ronan et al, 2013; Son & Crabtree, 2014; Choi et al, 2015; Alfert et al, 2019). To delineate the expression profile of SWI/SNF/BAF complex subunits that are part of the core and ATPase modules (Fig 1A and B), we initially employed mouse-derived embryonic stem cells (ESCs), embryonic neural progenitor cells (eNPCs), and primary cortical neurons (CNs, 7 days in vitro; Fig 1C). As a complementary in vitro models, we then used iPSCs, iPSC-derived smNPCs, and smNPC-derived neurons (Fig 1D). We quantified the expression of selected SWI/SNF/BAF complex subunits and observed a consistent upregulation of BAF170, BCL7A, and BAF60C during the differentiation of ESCs and iPSCs to NPCs and immature neuronal cells (Fig 1C and D). Contrary to BCL7A, the expression of BCL7-family member BCL7B gradually decreased during neuronal differentiation (Fig 1C and D).

Earlier studies have clarified the contribution of BAF170 to stem cell maintenance and neurogenesis in mammals (Kaeser et al, 2008; Tuoc et al, 2013, 2017; Alajem et al, 2015; Narayanan et al, 2015; Bachmann et al, 2016). Similarly, BAF60A/B/C are known to take part in cell fate specification, including ESC differentiation (Alajem et al, 2015) as well as cardiac and skeletal myogenesis (Puri & Mercola, 2012; Toto et al, 2016). In contrast, while BCL7A has been previously described in tumorigenesis (Zani et al, 1996; Ramos-Medina et al, 2013; Balinas-Gavira et al, 2020), its participation in neurogenesis remains unknown.

Prior evidence showed that BCL7A is part of the ATPase module and may influence BRM/BRG1 activity by enabling the efficient positioning and remodeling of the bound nucleosomes (Kadoch et al, 2013; Mashtalir et al, 2018, 2020; Fig 1E). To further confirm that BCL7A is fully incorporated in the SWI/SNF/BAF complex in both eNPCs and smNPCs, we performed co-immunoprecipitation (co-IP) analysis and revealed that BCL7A was pulled down using antibodies against either BRG1 or BAF170 (Fig 1F). Confocal imaging analyses of cultured cells showed that BCL7A is predominantly localized in the nucleus (Fig 1G), with its immunofluorescence intensity obviously
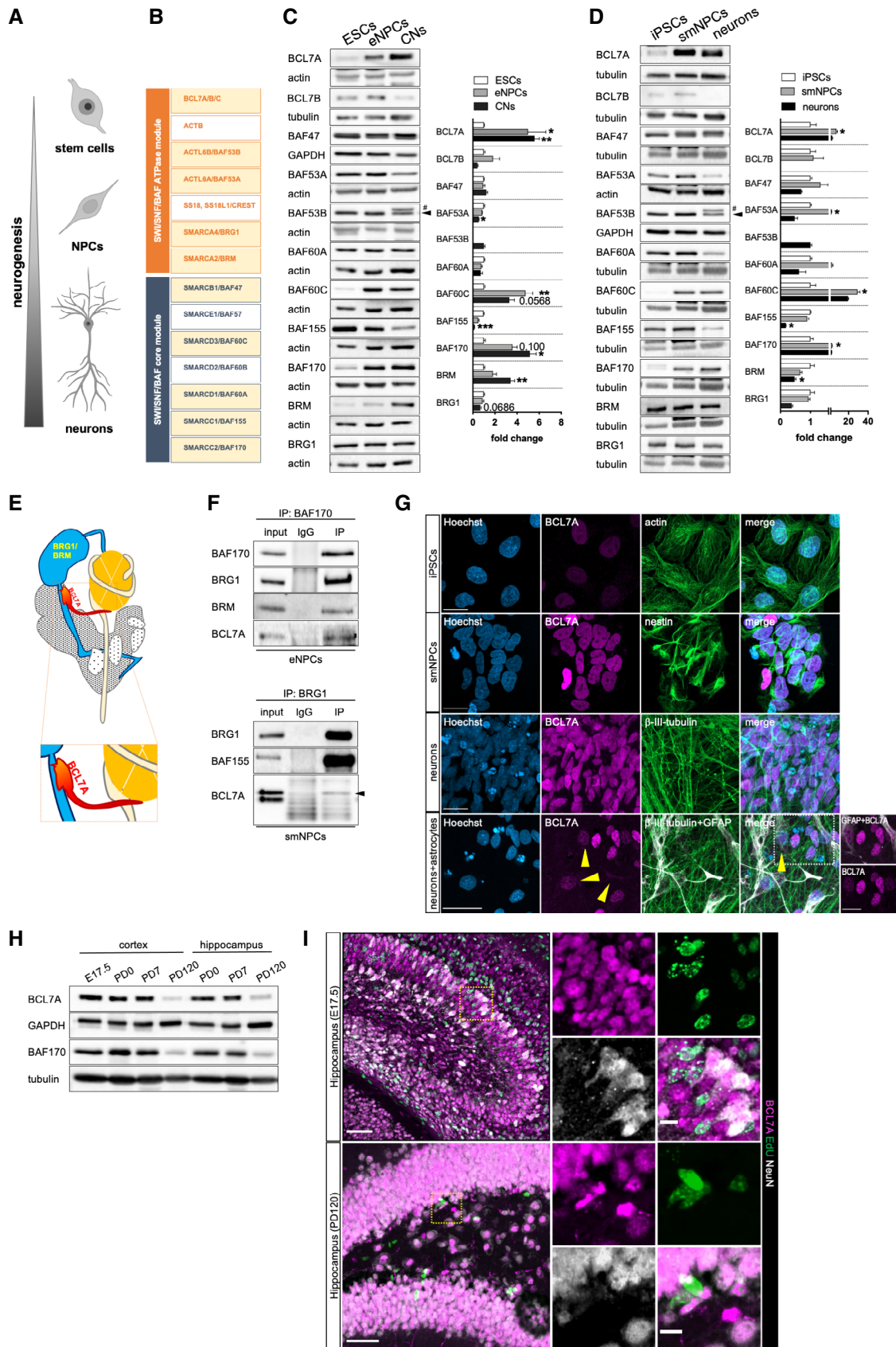
Figure 1.

Figure 1.   BCL7A is upregulated during NPC specification.

A   Schematic representation of stem cell differentiation into neural progenitors and subsequently into neurons.

B   Graphical summary of SWI/SNF/BAF complex subunits that are part of the ATPase (orange) or core (dark blue) modules. Highlighted in yellow are the subunits that have been assessed by immunoblot analyses.

C, D   Representative western blots and respective densitometries (right panel) for the selected SWI/SNF/BAF complex subunits ($n = 3$–5 biological replicates). Arrow heads indicate nonspecific bands, while # symbol highlights BAF53B.

E   Schematic representation of nucleosome-bound SWI/SNF/BAF complex. BCL7A is stably incorporated in the ATPase module, with amino acids residues at the N-terminus of BCL7A interacting with BRM/BRG1 or with H2A/H2B dimers.

F   Representative immunoblots of co-immunoprecipitation (co-IP) experiments in eNPCs (top panels) and smNPCs (bottom panels). Co-IPs were performed with anti-bodies against BAF170 (top) and BRG1 (bottom). Inputs are homogenates from eNPCs (left) and smNPCs (right). IgG indicates IgG-bound Sepharose beads (as controls), while IP indicates immunoprecipitated samples after elution from the beads. Arrow head indicates BCL7A band at the correct MW.

G   Immunofluorescence staining of BCL7A (purple) along with actin, nestin, and β-III tubulin (green) as well as GFAP (white) in iPSCs, smNPCs, and smNPC-derived neurons and astrocytes, respectively. Arrow heads indicate GFAP-positive glial cells with low BCL7A expression. Scale bars = 20 μm.

H   Western blot analysis of BCL7A and BAF170 in cortex and hippocampus of embryonic (E17.5), early postnatal (PD0 and PD7), and adult (PD120) mouse brain tissue showing a progressive temporal reduction of protein levels in the analyzed tissues.

I   Immunofluorescence staining of BCL7A (purple), EdU (green), and NeuN (white) in embryonic (E17.5) and adult (PD120) hippocampal brain sections. EdU was used to label proliferating NPCs, whereas NeuN was used as a neuronal marker. Scale bars = 50 μm (left panels) and 10 μm (right panels).

Data information: Data are presented as mean ± SEM. Kruskal–Wallis test was used in (C) and (D): *$P < 0.05$, **$P < 0.01$.

Source data are available online for this figure.

---

increasing during NPC differentiation toward neurons, while scarcely detectable in GFAP-positive cells. In the mouse brain, BCL7A expression peaked between embryogenesis and the first week after birth, whereas it diluted in adult tissues (Fig 1H). We additionally carried out confocal microscopy of brain slices from E17.5 embryos and adult mice that were treated with 5-ethynyl-2′-deoxyuridine (EdU) to label proliferating neural stem and progenitor cells (Fig 1I). We detected BCL7A expression in the nucleus of NeuN-positive neurons but also in NeuN-negative/EdU-positive cells (Fig 1I). Together, these findings indicate that BCL7A is highly expressed in cultured NPCs and neurons as well as in dividing and postmitotic cells within the DG of the mouse brain.

BCL7A stimulates SWI/SNF/BAF complex occupancy at target genomic regions in NPCs

To determine the mechanistic contribution of BCL7A to cell type specification, we generated wt and BCL7A KO eNPCs from our transgenic mouse lines (Wischhof *et al*, 2017). Additionally, we obtained two iPSC lines (from herein indicated as KO$_1$ and KO$_2$) genetically modified for BCL7A expression using a CRISPR/Cas9 method. The 8 bp deletion and 1 bp deletion in KO$_1$ and KO$_2$,

respectively, caused frameshifts in exon 2, resulting in homozygous *null* alleles due to premature stop codons (Appendix Fig S1A and B). In proliferating iPSCs, BCL7A loss inhibited the expression of pluripotency markers (*NANOG*, *OCT4*, and *FGF4*; Appendix Fig S1C) and altered the spontaneous differentiation of embryoid bodies into the three germ layers (Appendix Fig S1D–F). In this regard, the expression profiles of markers associated with ectoderm and endoderm were significantly different in BCL7A KO embryoid bodies (Appendix Fig S1F), possibly suggesting aberrant tissue morphogenesis and/or maturation states of cells within these transient structures. These data provide a first hint on the putative contribution of BCL7A to cell stemness and differentiation.

Genetic manipulation of *BCL7A* alleles in both eNPCs and smNPCs abrogated BCL7A protein expression (Fig 2A and B) without altering the immunocytochemical profile of neural stem cell markers (i.e., nestin and SOX2) or cell proliferation as revealed by EdU incorporation (Appendix Fig S1G and H). We assessed the expression of selected SWI/SNF/BAF complex subunits (BRG1, BAF170, and BAF155) and found negligible differences in control versus BCL7A KO cells (Fig 2C and D). To determine whether BCL7A loss could affect SWI/SNF/BAF complex stability, we performed density sedimentation and co-IP assays on nuclear

---

Figure 2.   Loss of BCL7A in NPCs alters SMARCA4/BRG1 occupancy at the TSS of genes associated with neuronal differentiation.

A   Immunoblot and immunofluorescence staining of BCL7A (red) in eNPCs isolated from *Bcl7a*$^{wt/wt}$ (wt) and *Bcl7a*$^{ko/ko}$ (ko) embryos (E13.5). Nestin (green) was used as NPC marker, whereas DAPI (blue) was used to stain nuclei. Scale bar = 10 μm.

B   Immunoblot and immunofluorescence staining of BCL7A in smNPCs. Two different BCL7A knockout clones (KO$_1$ and KO$_2$) were used along with the parental (P) cell line. Scale bar = 10 μm.

C, D   Representative western blots and respective densitometries (right panel) for selected SWI/SNF/BAF complex subunits in (C) eNPCs ($n = 4$ biological replicates) and (D) smNPCs ($n = 3$–6 biological replicates).

E–G   BCL7A KO and wt smNPCs were used for (F) nuclear isolation followed by density sedimentation and (G) differential salt extraction. Top panels show representative immunoblots for selected SWI/SNF/BAF complex subunits and respective densitometries are shown below ($n = 3$ biological replicates).

H, I   Heatmaps of SMARCA4/BRG1 and H3K27me3 ChIP-seq in wt and BCL7A KO eNPCs.

J   Average density plots for SMARCA4/BRG1 occupancy around the TSS in wt and BCL7A KO eNPCs.

K, L   Heatmaps of SMARCA4/BRG1 and H3K27me3 ChIP-seq in parental and BCL7A KO smNPCs.

M   Average density plots for SMARCA4/BRG1 occupancy around the TSS in parental and BCL7A KO smNPCs.

N, O   Simplified ClueGO pathway analysis of enriched GO terms (Biological Processes) performed on genes with reduced SMARCA4/BRG1 occupancy (FC > 1) at promoter regions in (N) BCL7A KO vs. wt eNPCs and (O) BCL7A KO clones compared to parental smNPCs.

Data information: Data in (C), (D), and (G) are presented as mean ± SEM.
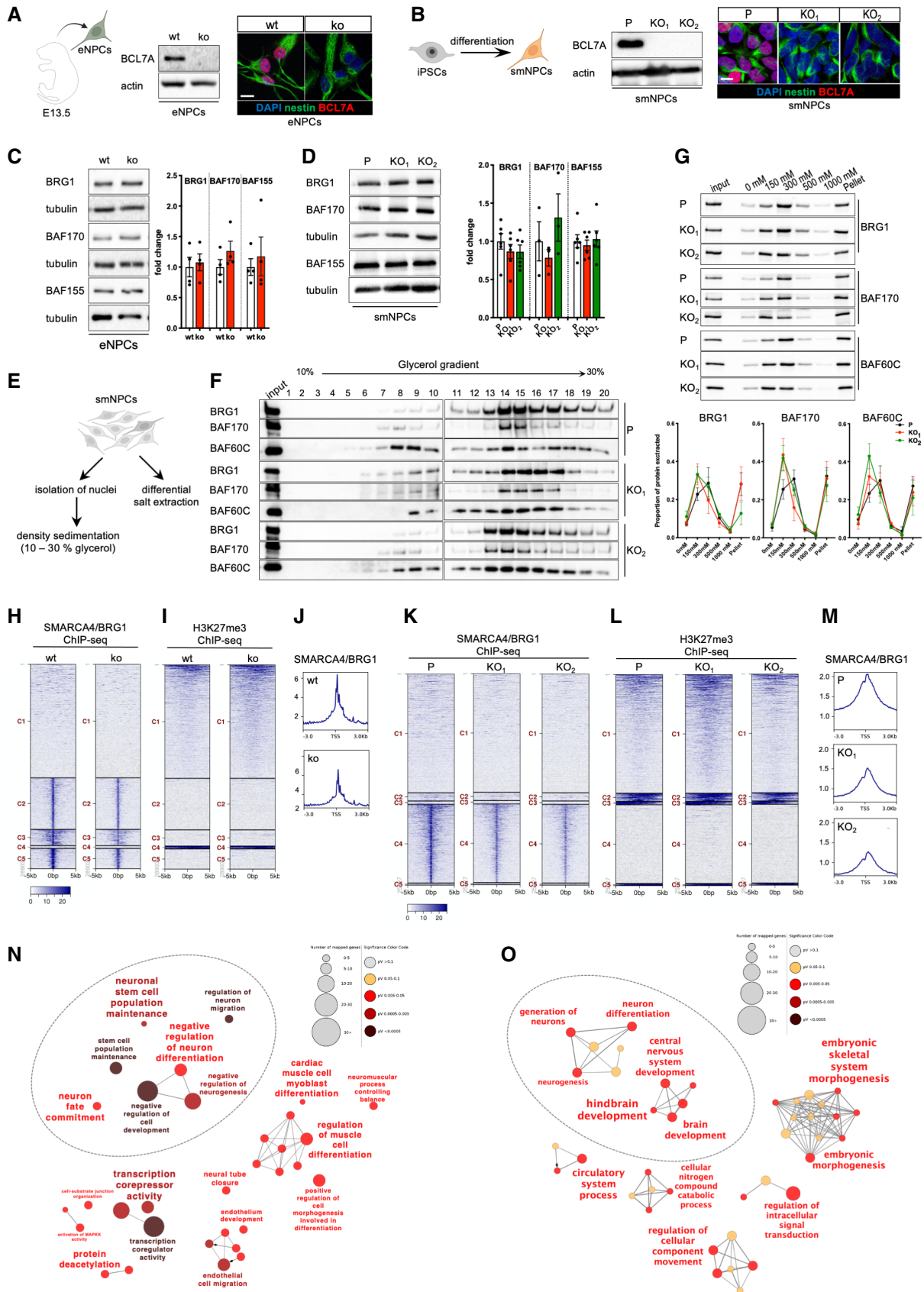
Source data are available online for this figure.

Figure 2.

extracts (Fig 2E and F, and Appendix Fig S1I). Density sedimentation assay using 10–30% glycerol gradients did not reveal major differences in migration patterns of SWI/SNF/BAF complex components (Fig 2F). Consistently, immunoprecipitation of SWI/SNF/BAF complexes from nuclear extracts and subsequent silver staining showed no major changes in BCL7A KO samples compared to controls (Appendix Fig S1I). At least in NPCs, these data indicate that BCL7A plays a minor role in the SWI/SNF/BAF complex integrity.

As SWI/SNF/BAF complexes contain several subunits with DNA- and histone-binding domains (Mashtalir *et al*, 2018; Valencia & Kadoch, 2019), we next sought to determine whether BCL7A KO alters SWI/SNF/BAF complex affinity to chromatin. We performed differential salt extraction and found that BCL7A-deficient SWI/SNF/BAF complexes dissociate from chromatin at slightly lower salt concentrations, indicating a decreased chromatin affinity (Fig 2G). As BCL7A loss may influence SWI/SNF/BAF chromatin occupancy, we next sought to determine the SWI/SNF/BAF complex distribution at targeted genomic regions. Since BRG1 expression remains relatively stable in ESCs, iPSCs, eNPCs, and smNPCs (Figs 1C and D, and 2C and D), we performed chromatin immunoprecipitation (ChIP) followed by genome-wide sequencing using a previously validated antibody against SMARCA4/BRG1. Remarkably, BRG1 ChIP-seq on control versus BCL7A KO cells revealed that BCL7A enabled genome-wide BRG1 occupancy in a consistent manner in both mouse eNPCs and human smNPCs (total number of peaks identified: 20,880 in wt eNPCs; 27,157 in BCL7A KO eNPCs; 16,917 in parental smNPCs; 13,681 and 13,180 in BCL7A KO$_1$ and KO$_2$ smNPCs, respectively; Figs 2H–M and EV1A–J). Specifically, we found that BCL7A KO led to a substantial reduction of BRG1 binding at transcriptional starting sites (TSS $\pm$ 1 kb) and putative enhancers (defined by regions with strong H3K4me1 enrichment). Despite this global decrease in BRG1 enrichment, a subset of genes showed an enhanced SMARCA4/BRG1 binding at promoters or putative enhancer regions in BCL7A KO mouse eNPCs, whereas only very few genes showed increased BRG1 binding in BCL7A KO smNPCs (Fig EV1C, D, I, and G, H, J). Since SWI/SNF/BAF complexes can exert their activity in part through epigenetic antagonism of PRC (Ronan *et al*, 2013; Kadoch *et al*, 2016, 2017; Bracken *et al*, 2019), we performed a ChIP-seq study of the repressive mark H3K27me3 established by PRC2 (Zhang *et al*, 2015; Kadoch *et al*, 2016). We found the most pronounced H3K27me3 enrichment at genomic loci with only very sparse or absent BRG1 binding in both wt and KO cells (total number of peaks identified: 30,813 in wt and 32,511 in BCL7A KO eNPCs; 22,649 in parental smNPCs; 29,137 and 26,170 in BCL7A KO$_1$ and KO$_2$, respectively; cluster C1 and C4 in Fig 2H and I; clusters C1–C3 and C5 in Fig 2K and L). In BCL7A-deficient eNPCs and smNPCs, we observed one set of genes with little BRG1 binding but with only slightly increased H3K27me3 (cluster C1 in Fig 2H–L). However, altered BRG1 occupancy did not seem to directly influence H3K27me3 distribution in BCL7A KO eNPCs and smNPCs (Fig EV1C, D, G and H), as regions/genes with differential BRG1 enrichment did not simultaneously gain or lose H3K27me3 (clusters C2–C3 and C5 in Fig 2H and I as well as cluster C4 in Figs 2K and L, and EV1C, D, G and H). These findings suggest that the detected changes seen in H3K27me3 enrichment are rather secondary as opposed to a direct consequence of reduced BRG1 binding. To investigate functionally grouped gene ontology (GO) and explore molecular networks as interconnected nodes and edges, we

performed ClueGO analysis of BRG1-targeted TSS that were significantly dysregulated in BCL7A-deficient cells compared to controls. In murine BCL7A KO eNPCs, we identified a cluster of enriched genes that negatively regulates neuronal stem cell maintenance and neuronal differentiation as well as cell commitment, neuron migration, and neurodevelopment (Figs 2N and EV1K). We carried out a parallel ClueGo analysis with data from human smNPCs and observed a similar pathway enrichment (Figs 2O and EV1L). Importantly, we also identified an additional cluster of genes primarily involved in catabolic processes, possibly implying a role of BCL7A also in metabolism (Fig 2O). Together, these data suggest that BCL7A stimulates BRG1 occupancy at target genes that may potentially influence neuronal specification and differentiation.

Additionally, we tested whether BCL7A KO could influence SWI/SNF/BAF complex distribution at targeted genomic regions in nonneuronal cells. To do so, we employed near-haploid tumorigenic wt and BCL7A KO HAP1 cells (Schick *et al*, 2019) and performed ChIP-seq analysis (total number of peaks identified: 9,335 in wt and 10,098 in BCL7A KO HAP1 cells; Appendix Fig S2A). We observed a clear redistribution of SMARCA2/BRM-containing SWI/SNF/BAF complexes in tumorigenic BCL7A KO HAP1 cells (Appendix Fig S2B), with less intense and broader peaks in BCL7A KO cells (Appendix Fig S2C) that suggested a weaker binding to targeted regions. Of note, ClueGO analysis of genes with differentially regulated BRM binding upon BCL7A loss predicted an enrichment of pathways involved in mitochondrial function among others (Appendix Fig S2D and E). These data suggest that BCL7A loss can result in SWI/SNF/BAF re-targeting in a biological context-dependent manner and further point toward a potential contribution of BCL7A-containing SWI/SNF/BAF complexes in cellular metabolism.

BCL7A loss skews NPC specification toward gliogenesis

To provide a causal link between BCL7A and NPC differentiation, we assessed neuro-gliogenesis by performing several *in vitro* and *in vivo* experiments. Wt and BCL7A KO eNPCs were spontaneously differentiated for 8 days by withdrawing growth factors, then samples were collected at different time points for subsequent immunoblots. Compared to controls, BCL7A KO cultures exhibited a lower expression of the neuronal marker β-III tubulin, which inversely correlated with a significant time-dependent increase of astrocytic GFAP protein (Figs 3A and EV2A), while we only observed a slight decrease in SOX10$^+$ oligodendrocytes (Fig EV2A). Sholl analysis of β-III tubulin-stained cells at 7 days of differentiation revealed a reduced neurite complexity of BCL7A KO compared to wt cells (Fig 3B). To corroborate this evidence, we spontaneously differentiated human smNPCs for 30 days and immunostained the resulting mixed cultures. In line with our results in eNPC cultures, BCL7A KO clones exhibited an evident reduction of β-III tubulin staining associated with an increased number of GFAP-positive cells (Fig 3C). In differentiating BCL7A-deficient cells, *TUBB3* and *GFAP* mRNA levels were downregulated and upregulated, respectively (Fig 3C). We reasoned that other BCL7-family members (i.e., BCL7B and BCL7C) might phenocopy BCL7A deficiency. Since BCL7B is almost 100 times more highly expressed than BCL7C in mouse brain tissues (Wischhof *et al*, 2017), we subjected mouse-derived BCL7B KO eNPCs to spontaneous differentiation. While we did not find any
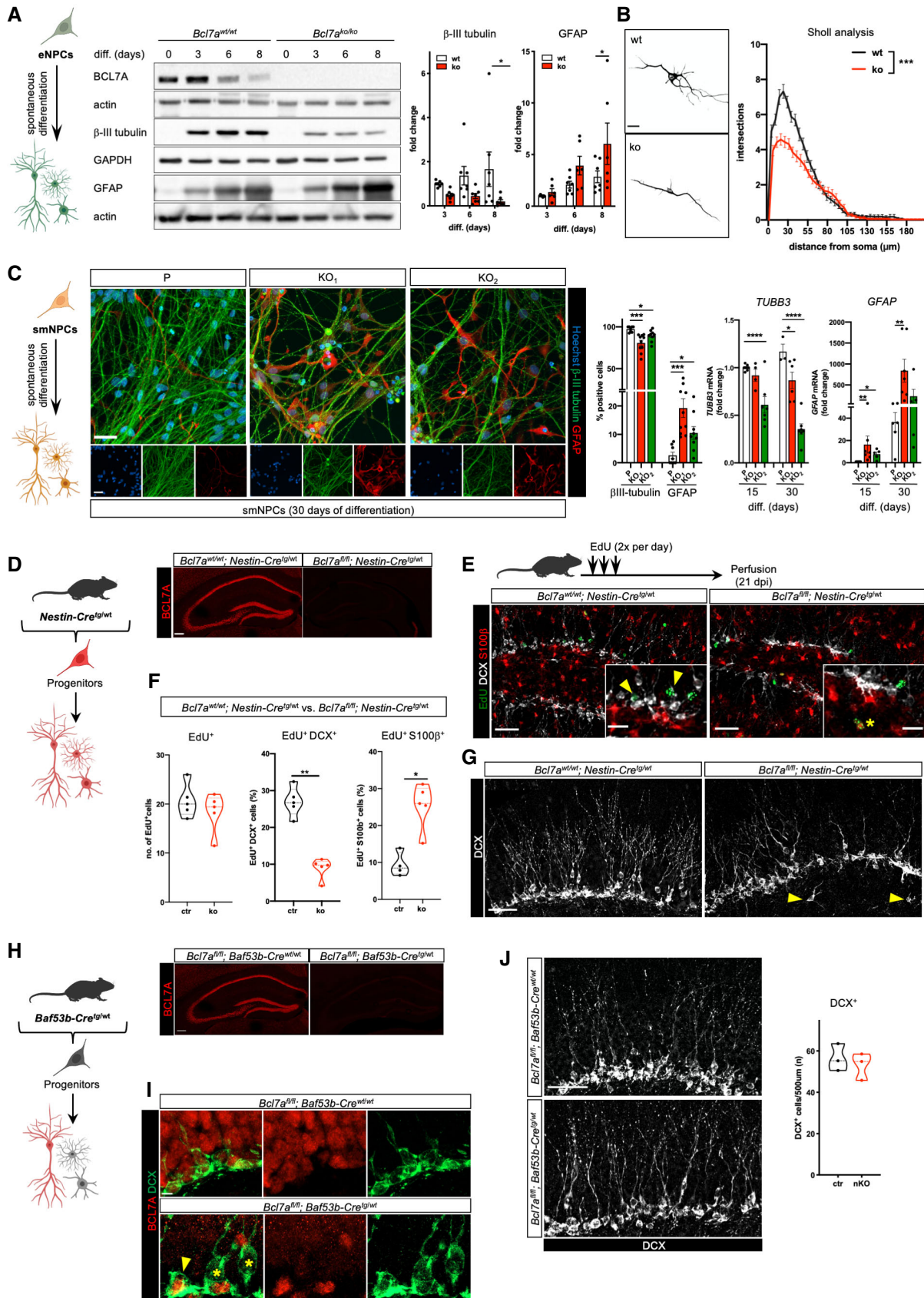
Figure 3.

◀

Figure 3. Lack of BCL7A impairs neurogenesis and reduces neurite complexity of differentiating neurons *in vitro* and *in vivo*.

A   Immunoblots of spontaneously differentiated wt and BCL7A KO eNPCs. Samples were collected at the indicated differentiation time points. Respective densitometries are shown on the right (n = 6–7 biological replicates).

B   Sholl analysis of β-III tubulin-positive immature wt and BCL7A KO neurons following 7 days of spontaneous eNPC differentiation (n = 4 biological replicates, each experiment with 10–15 cells per condition). Scale bar = 20 μm.

C   Immunofluorescence staining (central panel) and quantification (right panel) of β-III tubulin- and GFAP-positive cells as well as RT-PCR analysis (right panels) of spontaneously differentiated iPSC-derived parental and BCL7A KO smNPCs (n = 3–7 biological replicates). Scale bar = 50 μm.

D   Immunofluorescence staining of BCL7A expression in hippocampal sections from adult control and *Bcl7a$^{fl/fl}$; Nestin-Cre$^{tg/wt}$* mice. Scale bar = 200 μm.

E   EdU experiments in adult mice. Animals were injected with EdU twice daily for 3 days and sacrificed 21 days thereafter. Images show immunofluorescence stainings for EdU (green), doublecortin (DCX, white), and S100β (red) in hippocampal brain sections from *Bcl7a$^{wt/wt}$; Nestin-Cre$^{tgt/wt}$* (as control) and *Bcl7a$^{fl/fl}$; Nestin-Cre$^{tg/wt}$* mice. Representative EdU$^+$ DCX$^+$ (yellow arrow heads) or EdU$^+$ S100β$^+$ (yellow asterisk) double-labeled cells are indicated in the insets. Scale bar = 50 and 20 μm (for insets).

F   Quantification of EdU$^+$ (left panel), EdU$^+$ DCX$^+$ (middle panel), and EdU$^+$ S100β$^+$ (right panel) cells within the hippocampal dentate gyrus (DG) of adult control (n = 4) and *Bcl7a$^{fl/fl}$; Nestin-Cre$^{tg/wt}$* (n = 5) animals.

G   Immunofluorescence staining for DCX$^+$ cells within the DG region of adult *Bcl7a$^{fl/fl}$; Nestin-Cre$^{wt/wt}$* (as control) and *Bcl7a$^{fl/fl}$; Nestin-Cre$^{tg/wt}$* animals. Confocal imaging analysis shows a lower number, misalignment, and reduced neuritic complexity of DCX$^+$ labeled cells in BCL7A KO mice compared to controls. Yellow arrows indicate misaligned DCX$^+$ cells. Scale bar = 50 μm.

H   Immunofluorescence staining of BCL7A (red) of hippocampal sections from *Bcl7a$^{fl/fl}$; Baf53b-Cre$^{wt/wt}$* (as control) and *Bcl7a$^{fl/fl}$; Baf53b-Cre$^{tg/wt}$* mice. Scale bar = 200 μm.

I   Immunofluorescence staining of BCL7A (red) and DCX (green) in hippocampal sections of control and *Bcl7a$^{fl/fl}$; Baf53b-Cre$^{tg/wt}$* mice. Yellow arrow indicates dividing cells, whereas yellow asterisks mark differentiating immature neurons. Scale bar = 5 μm.

J   Immunofluorescence staining for DCX (white) within the DG region of adult control and *Bcl7a$^{fl/fl}$; Baf53b-Cre$^{tg/wt}$* mice. Representative images show no obvious difference in number, morphology or alignment of DCX$^+$ labeled cells. Quantification of DCX$^+$ labeled cells in control and *Bcl7a$^{fl/fl}$; Baf53b-Cre$^{tg/wt}$* mice is shown on the right (n = 3 per genotype). Scale bar = 50 μm.

Data information: Data are presented as mean ± SEM. In (A) and (B), two-way ANOVA and two-way RM ANOVA, respectively, were used followed by Bonferroni's *post hoc* test for multiple comparisons. One-way ANOVA was used in (C) while in (F) and (J), unpaired two-sided Student's *t* test was used. *P < 0.05, **P < 0.01, ***P < 0.001, ****P < 0.0001.

Source data are available online for this figure.

differences between BCL7B KO and control cells regarding the number of β-III tubulin$^+$ neurons (Fig EV2B and C), differentiated BCL7B KO cells showed a slightly decreased percentage of GFAP$^+$ astrocytes together with a remarkable increase of SOX10$^+$ oligodendrocytes (Fig EV2C). Of note, we observed significantly higher BCL7A immunoreactivity in β-III tubulin-positive cells compared to GFAP-positive glia, while BCL7B expression levels appeared to be similar in both cell types (Fig EV2D and E). Thus, BCL7B does not seem to take part in neuronal differentiation, although it can contribute to oligodendrogenesis as recently suggested (Iram *et al*, 2022).

Next, we crossed *Bcl7a$^{fl/fl}$* mice with a line expressing a Cre-recombinase under the control of the *Nestin* promoter (i.e., *Nestin-Cre$^{tg/wt}$*), hence obtaining animals in which *Bcl7a* was conditionally deleted in neural stem cells. Loss of BCL7A protein expression within different brain regions was confirmed by immunohistochemical, western blot, and RT-PCR analyses (Figs 3D, and EV3A and B). In adult mice, *Bcl7a* KO led to a significant upregulation of *Bcl7b* and *Bcl7c* in the cerebellum and in the cortex, respectively, although it did not alter *Bcl7b* and *Bcl7c* expression in the hippocampus (Fig EV3B).

We initially assessed cortex development in *Bcl7a$^{fl/fl}$; Nestin-Cre$^{tg/wt}$* pups. To label embryonic NPCs, we therefore injected pregnant females with EdU during mid-neurogenesis (E14.5–15.5) and sacrificed the respective offspring 3 days after birth. While *Bcl7a$^{fl/fl}$; Nestin-Cre$^{tg/wt}$* pups showed a slight increase in the number of cells positive for EdU and negative for the neuronal marker NeuN as well as cells double-positive for EdU and S100β (astrocyte marker), these changes were mild and did not result in an obvious reduction of the cortical thickness (Fig EV3C and D). We further observed a higher percentage of GFAP-immunoreactivity in the cortex of *Bcl7a$^{fl/fl}$; Nestin-Cre$^{tg/wt}$* animals at PD6 (Fig EV3E), yet there was no significant change in terms of cortical thickness. It has been previously suggested that the *Nestin-Cre* line is insufficient for recombination in

early embryonic progenitors and results in sufficient recombination only during the early postnatal period (Liang *et al*, 2012). We therefore speculate that the mild effect on cortical neurogenesis observed in *Bcl7a$^{fl/fl}$; Nestin-Cre$^{tg/wt}$* animals may be due to incomplete recombination of the floxed alleles. In support of our argument, P3 *Bcl7a$^{fl/fl}$; Nestin-Cre$^{tg/wt}$* brains showed several BCL7A positive cells within the cortex and hippocampus (Fig EV3A), whereas BCL7A immunoreactivity appeared to be absent in adult *Bcl7a$^{fl/fl}$; Nestin-Cre$^{tg/wt}$* mice (Fig 3D). However, additional immunohistochemical analysis at different embryonic and perinatal timepoints would need to be done in order to determine when the deletion of *Bcl7a* occurs. We went on to evaluate *in vivo* proliferation and differentiation of adult NPCs using 3–4 months-old *Bcl7a$^{fl/fl}$; Nestin-Cre$^{tg/wt}$* and control littermates. After EdU injections (100 μg/kg body weight, i.p), animals were then sacrificed either 24 h (i.e., proliferation experiment) or 21 days (i.e., differentiation experiment; Figs 3E and EV4F). The total number of EdU$^+$-labeled cells did not differ between *Bcl7a$^{fl/fl}$; Nestin-Cre$^{tg/wt}$* and control mice, suggesting that loss of BCL7A has no effect on either the proliferation or survival of adult NPCs (Figs 3E and F, and EV3F). Interestingly, conditional *Bcl7a* KO animals showed a significant reduction of doublecortin-positive (DCX$^+$) as well as EdU$^+$ DCX$^+$ double-labeled cells along with a significantly higher number of cells that were double-positive for EdU and S100β (as a marker of astrocytes; Fig 3E and F). We further noticed that DCX$^+$ cells were misaligned with respect to the granule cell layer of the DG in *Bcl7a$^{fl/fl}$; Nestin-Cre$^{tg/wt}$* mice (Figs 3G and EV3F), possibly indicating defects in migration and integration into existing neural circuits. Of note, BCL7B KO mice did not show detectable changes in EdU$^+$ and DCX$^+$ cell numbers compared to control littermates (Fig EV4A), further indicating that BCL7B is dispensable for adult neurogenesis. Interestingly and in support of our *in vitro* observations (Fig EV2C), BCL7B KO mice showed a

higher number of cells double-positive for EdU and the oligodendrocyte marker SOX10, further pointing toward a possible role for BCL7B in oligodendrogenesis (Fig EV4B). Taken together, BCL7A loss has negligible effects on adult NPC proliferation, however it skews NPC specification toward glial differentiation *in vitro* and *in vivo*.

In addition to a lower percentage of EdU$^+$ DCX$^+$ double-labeled cells, BCL7A KO cells showed a reduced complexity of the dendritic branching (Fig 3G). To determine whether the observed neurite defects were caused by BCL7A deficiency in NPCs (i.e., prior to exiting the cell cycle), we crossed *Bcl7a$^{fl/fl}$* mice with a line expressing a Cre-recombinase under the control of the *Baf53b* promoter (i.e., *Baf53-Cre$^{tg/wt}$*), knowing that *Baf53b* is primarily expressed in postmitotic developing neurons (Zhan *et al*, 2015). Confocal imaging analysis confirmed that BCL7A was still detectable in proliferating neuroblasts (i.e., DCX$^+$ cells lacking neurite outgrowth) and GFAP$^+$ astrocytes, however it was lost in postmitotic neurons in *Bcl7a$^{fl/fl}$*; *Baf53b-Cre$^{tg/wt}$* brain sections (Figs 3H and I, and EV4C). Compared to controls, *Bcl7a$^{fl/fl}$*; *Baf53b-Cre$^{tg/wt}$* DG did not show any obvious changes in either the number or pattern alignment of newly differentiated DCX$^+$ cells (Fig 3J). These *in vivo* data indicate that BCL7A expression in NPCs, rather than in postmitotic cells, is crucial for proper maturation and integration of adult-born neurons.

BCL7A KO alters glutamatergic signaling and mouse behavior

To explore cellular processes linked to BCL7A, we reviewed our SMARCA4/BRG1 ChIP-seq data and performed additional GO analysis for cellular components. Since ClueGo analysis predicted aberrant glutamatergic signaling in BCL7A KO tissues (Fig 4A), we set out to run conventional calcium (Ca^{2+}) measurements using Fluo-4 loaded mouse-derived cortical neurons bathed in a glycine-containing and Mg^{2+}-free buffer (Bano *et al*, 2010; Ziviani *et al*, 2011). Compared to controls, BCL7A KO cells had a much lower

Ca^{2+} rise upon glutamate exposure (Fig 4B). Similarly, 100 µM glutamate treatment elicited significantly smaller intracellular Ca^{2+} transients in smNPC-derived BCL7A KO neuronal cultures compared to wt cells (Fig 4C). To corroborate this evidence, we extracted proteins from *Bcl7a$^{fl/fl}$*; *Nestin-Cre$^{tg/wt}$* and control littermates and ran immunoblot analyses using antibodies against ionotropic NMDA receptor subunits (i.e., NMDAR1, NMDAR2A, NMDAR2B) and synapsin (SYN1), a protein highly associated to synaptic vesicles. Consistent with an aberrant glutamatergic system, we found a reduced expression of NMDAR1, NMDAR2A, and SYN1 in hippocampal tissues from adult *Bcl7a$^{fl/fl}$*; *Nestin-Cre$^{tg/wt}$* mice compared to controls (Fig 4D). To investigate the downstream consequences of these alterations, we next assessed changes in the expression levels of cFos, an accepted proxy of activity-dependent gene transcription (Dragunow & Faull, 1989; Sheng & Greenberg, 1990; Madabhushi *et al*, 2015), in smNPC-derived BCL7A KO and control neurons (Fig 4E). While glutamate stimulation resulted in a strong upregulation of *FOS* mRNA in control cells (approximately 1,000% increase relative to baseline levels), this response was significantly reduced in BCL7A KO neurons (Fig 4E). To support these *in vitro* observations, we then performed cFos immunostainings in *Bcl7a$^{fl/fl}$*; *Baf53b-Cre$^{tg/wt}$* and control mice that had been briefly exposed to an enriched environment (EE), as a means to stimulate neuronal activity. An additional mouse cohort was kept in standard home cage condition and was used as control to establish the baseline of cFos immunoreactivity. While control mice exposed to EE showed a significant increase in cFos immunoreactivity within the DG, the number of cFos$^+$ cells did not significantly differ between home cage and EE housed animals lacking BCL7A (Fig 4F). These data suggest that BCL7A deficiency compromises the glutamatergic system and the physiologically linked gene transcription underlying neuronal plasticity.

Since aberrant Ca^{2+} signaling as well as activity-dependent gene transcription often correlate with behavioral abnormalities, we set

---

Figure 4. BCL7A loss alters neuronal activity and mouse behavioral performance.

A   Simplified ClueGO pathway analysis of genes with reduced SMARCA4/BRG1 occupancy at promoter regions in BCL7A KO vs. wt eNPCs.

B, C   Representative Ca^{2+} measurements in (B) wt vs. BCL7A KO cortical neurons (CN, 10 days *in vitro*) and in (C) smNPC-derived parental and BCL7A KO neurons. Ca^{2+} changes were detected using Fluo-4 and upon treatment with (B) 50 µM of glutamate (final concentration) and (C) 100 µM of glutamate (final concentration). Upper right panels report Ca^{2+} peaks (F) relative to baseline (F_0). In (B) wt: $n = 18$ cells; ko: $n = 23$ cells ($n = 2$ independent experiments). In (C) P: $n = 27$ cells; KO$_1$: $n = 20$ cells; KO$_2$: $n = 19$ cells ($n = 2$ independent experiments).

D   Immunoblot analysis of hippocampal tissues. Densitometries are shown on the right (ctr: $n = 4$–5 mice; ko: $n = 3$–4 mice).

E   RT-PCR analysis of *FOS* expression upon glutamate (100 µM for 10 min) stimulation in smNPC-derived parental and BCL7A KO neurons ($n = 5$–6 biological replicates).

F   Immunofluorescence staining of cFos in the dentate gyrus of adult *Bcl7a$^{fl/fl}$*; *Baf53b-Cre$^{tg/wt}$* (ko) mice and control (ctr) littermates. Mice were either kept in standard housing conditions (upper images; ctr: $n = 4$ mice; ko: $n = 4$ mice) or exposed to an enriched environment (lower images; ctr: $n = 6$ mice; ko: $n = 5$ mice). Quantification of cFos$^+$ cells are shown below. Scale bar = 30 µm.

G–K   Behavioral characterization of *Bcl7a$^{fl/fl}$*; *Nestin-Cre$^{tg/wt}$* (ko) mice compared to control (ctr) littermates. Animals were tested for their locomotor activity and coordination in (H) the open field (ctr: $n = 13$ mice; ko: $n = 11$ mice) and (I) RotaRod test (ctr: $n = 12$ mice; ko: $n = 7$ mice). Cognitive function was assessed in (J) the Y-maze spontaneous alternation task (ctr: $n = 13$ mice; ko: $n = 11$ mice) and (K) fear conditioning paradigm (ctr: $n = 11$ mice; ko: $n = 10$ mice). The percentage of spontaneous alternations and freezing were used as measures for working and long-term memory function, respectively.

L–Q   Behavioral characterization of adult *Bcl7a$^{fl/fl}$*; *Baf53b-Cre$^{tg/wt}$* (nKO) mice compared to control (ctr) littermates. Locomotor activity and coordination were assessed in (M) the open field (ctr: $n = 14$ mice; nKO: $n = 12$ mice) and (N) RotaRod paradigm (ctr: $n = 16$ mice; nKO: $n = 12$ mice). Cognitive function was tested in (O) the Y-maze (ctr: $n = 11$ mice; nKO: $n = 11$ mice) and (P, Q) Barnes maze test (ctr: $n = 11$ mice; nKO: $n = 11$ mice). Representative heatmaps of Barnes maze test are reported on the right. The time spent in target (^{T}) and nontarget quadrants during the probe trial are shown on the right.

Data information: Data are presented as mean ± SEM. In (B) and (D), Mann–Whitney test was used while in (H), (J), (K), (M), and (O), unpaired two-tailed Student's *t* test was used. Data in (C) and (E) were analyzed via Kruskal–Wallis test. In (F), (I), (N), (P), and (Q), two-way ANOVA, with repeated measures where appropriate, were done followed by Bonferroni's *post hoc* test for multiple comparisons. *$P < 0.05$, **$P < 0.01$, ***$P < 0.001$, ****$P < 0.0001$.
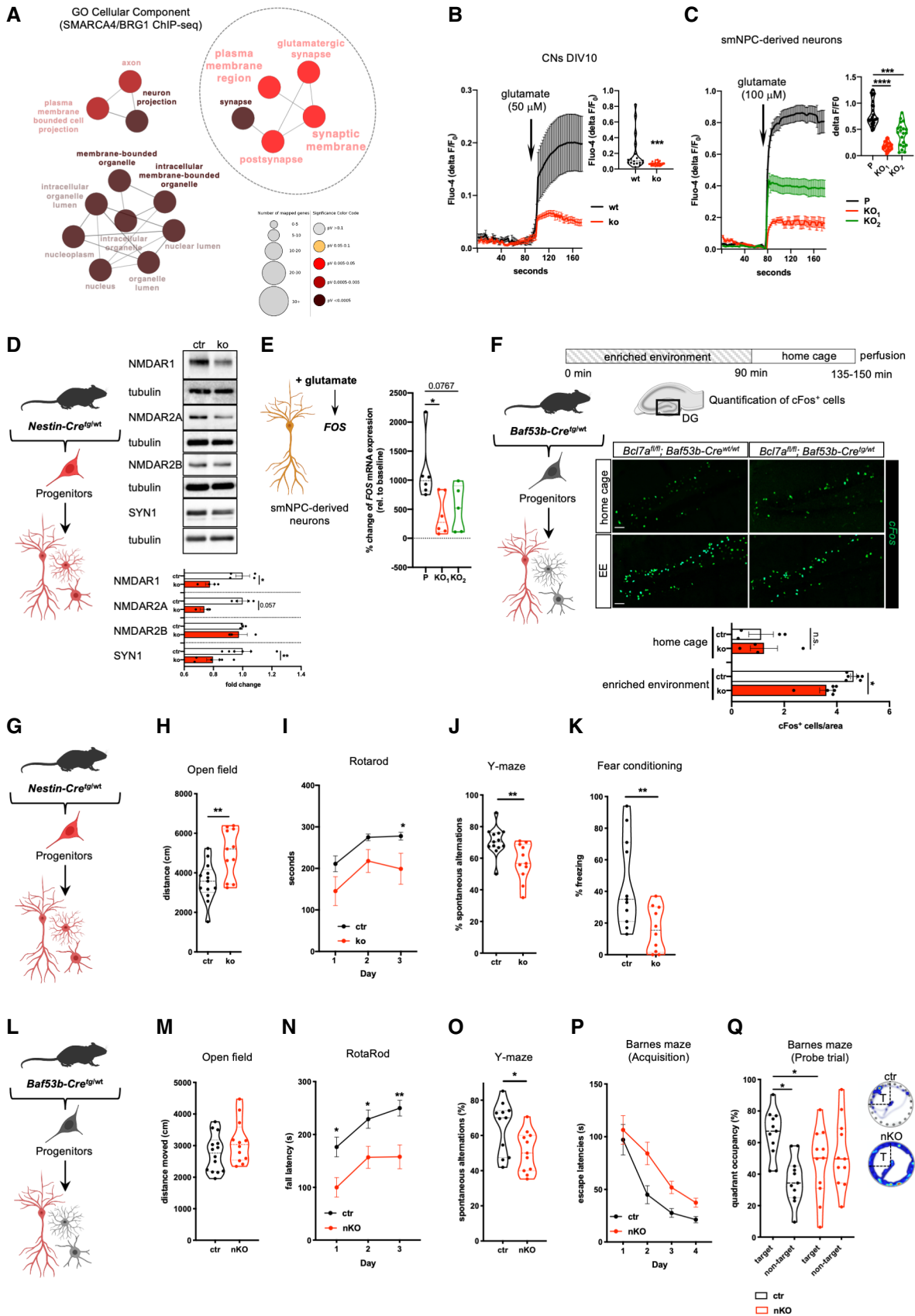Source data are available online for this figure.

Figure 4.

up an array of *in vivo* experiments in which *Bcl7a^{fl/fl}; Nestin-Cre^{tg/wt}* and control littermates underwent a variety of different behavioral paradigms (Fig 4G). Conditional BCL7A KO caused locomotor hyperactivity in the open field test and motor coordination deficits in the RotaRod paradigm (Fig 4H and I). We assessed the animals' spontaneous alternation behavior in the Y-maze test, which is thought to reflect cortex-dependent working memory function. We found that *Bcl7a^{fl/fl}; Nestin-Cre^{tg/wt}* mice showed a significantly reduced percentage of spontaneous alternations in comparison to control littermates, suggesting working memory impairments (Fig 4J). Additionally, animals were tested in the contextual fear conditioning paradigm, which mainly relies on hippocampus-dependent memory function. Here, conditional *Bcl7a* KO mice showed a strong reduction of freezing behavior during the retrieval trial (i.e., 24 h post conditioning), indicating deficits in hippocampus-dependent contextual fear memory (Fig 4K). Together, our experimental evidence suggests that embryonic BCL7A loss in NPCs alters behavioral performance, including cognitive function.

To determine whether behavioral defects can be elicited when *Bcl7A* deletion occurs during embryogenesis in postmitotic neurons, we generated control and *Bcl7a^{fl/fl}; Baf53b-Cre^{tg/wt}* mice that were subjected to an array of behavioral paradigms. We found that adult *Bcl7a^{fl/fl}; Baf53b-Cre^{tg/wt}* mice did not differ from control littermates in terms of locomotor activity in the open field (Fig 4L and M), however they still showed significant motor coordination deficits on the RotaRod (Fig 4N), consistent with our data in *Bcl7a^{fl/fl}; Nestin-Cre^{tg/wt}* mice (Fig 4I). In the Y-maze task, *Bcl7a^{fl/fl}; Baf53b-Cre^{tg/wt}* mice had fewer spontaneous alternations compared to control animals, suggesting a mild impairment of working memory (Fig 4O). Lastly, animals were trained and tested in the Barnes maze as a paradigm to assess hippocampus-dependent spatial learning and memory function. Animals were initially trained for 4 days during which escape latencies were recorded as a measure of training performance. Compared to control animals, *Bcl7a^{fl/fl}; Baf53b-Cre^{tg/wt}* mice showed a slightly, yet not significantly, slower performance improvement during the acquisition phase as indexed by longer escape latencies (Fig 4P). To assess long-term memory function, we performed a probe trial 72 h after the last training day. Here, the time spent in the target area, where the escape box was previously positioned, was used as a measure for memory function. While control mice showed a clear preference for the target over nontarget areas, *Bcl7a^{fl/fl}; Baf53b-Cre^{tg/wt}* animals spent equal time across all quadrants (Fig 4Q). Although milder compared to *Bcl7a^{fl/fl}; Nestin-Cre^{tg/wt}* mice, embryonic BCL7A KO in postmitotic cells can still cause deficits in hippocampus-dependent spatial memory function. Thus, loss of BCL7A in in immature neurons can still compromise motor coordination and cognitive function. Consistent with our previous findings (Wischhof *et al*, 2017), we can conclude that BCL7A expression promotes neurodevelopment and brain plasticity.

BCL7A determines cell type specification and neural differentiation through Notch and Wnt signaling

To gain further mechanistic understanding of BCL7A contribution to NPC differentiation toward neurons or glia, we performed mRNA sequencing (RNA-seq) of proliferating eNPCs. We found 599 differentially expressed genes (DEGs) in BCL7A KO cells compared to controls (Fig 5A). GO analysis of the 274 upregulated genes identified signatures of aberrant cell differentiation, neurogenesis, and brain development (Fig 5B), whereas GO of the 325 downregulated genes primarily identified changes in processes involved in glutamine catabolic process and ribosomal biology (Fig 5C). Ingenuity pathway analysis (IPA) predicted increased Notch signaling in proliferating BCL7A KO NPCs (Figs 5D and EV5A). Conversely, we observed that genes involved in the planar cell polarity (PCP) pathway (i.e., a noncanonical Wnt pathway independent of β-catenin) and canonical Wnt/β-catenin pathway were less represented in BCL7A-deficient cells (Figs 5D and EV5B). Given the relevance of Notch and Wnt pathways in NPC maintenance and differentiation (Zechner *et al*, 2003; Conboy *et al*, 2005; Lie *et al*, 2005; Ciruna *et al*, 2006; Mizutani *et al*, 2007; Kalani *et al*, 2008; Aguirre *et al*, 2010; Imayoshi *et al*, 2010; Pei *et al*, 2012), we investigated individual DEGs and found an upregulation of several Notch signaling components (i.e., *Dll1, Dll3, Dtx4, Hes5, Hey1, Mfng*, and

---

Figure 5. **BCL7A regulates cell type specification via Notch and Wnt signaling.**

A Heatmap of significantly dysregulated genes in BCL7A KO compared to wt eNPCs.

B, C GO terms of the top 10 biological processes for up- (B) and down-regulated (C) genes.

D List of the top 10 significantly enriched canonical pathways for up- and down-regulated genes.

E Heatmap of significantly dysregulated genes encoding components of the Wnt and Notch signaling pathways.

F Immunoblots of spontaneously differentiated wt and BCL7A KO eNPCs in presence of 1 μM of DAPT or 3 μM of CHIR99021.

G Immunofluorescence staining of eNPCs undergoing spontaneous differentiation for 7 days. BCL7A KO eNPCs were incubated for 72 h (24 h in proliferation plus 48 h in differentiation medium) with DMSO, 1 μM of DAPT, 3 μM of CHIR99021 or a combination of 1 μM of DAPT +3 μM of CHIR99021. Quantification of the β-III tubulin-positive or GFAP-positive cells is shown on the right ($n = 3$–6 technical replicates from three independent experiments). Scale bar = 50 μm.

H Sholl analysis of β-III tubulin-positive immature neurons after 7 days of spontaneous differentiation ($n = 4$ biological replicates with > 30 cells per condition). Scale bar = 20 μm.

I mRNA expression levels of *TUBB3* and *GFAP* at 15 and 25 days of spontaneously differentiating BCL7A KO compared parental smNPCs. BCL7A KO smNPCs were treated with DAPT, CHIR99021, DAPT + CHIR99021, or DMSO (as control = ctr) during the initial 7 days of spontaneous differentiation ($n = 3$–7 biological replicates).

J Immunoblots for non-phospho (active) β-catenin and TCF4/TCF7L2 in proliferating and 48 h-differentiated wt and BCL7A KO eNPCs. Respective densitometries are shown on the right ($n = 5$–8 biological replicates per condition).

K Scheme depicts Notch activation and Wnt inhibition in BCL7A KO NPCs. As a consequence of BCL7A deficiency, cells exhibit a decreased expression of β-catenin and TCF4/TCF7L2, which results in a negative feedback to Notch and Wnt pathways.

Data information: Data in (G), (H), (I), and (J) are presented as mean ± SEM. In (G) and (I), one-way ANOVA with Bonferroni's *post hoc* test for multiple comparisons was used while in (H), two-way RM ANOVA followed by Tukey's multiple comparisons test was performed. Data in (J) were analyzed via unpaired two-tailed Student's *t* test. *$P < 0.05$, **$P < 0.01$, ****$P < 0.0001$, ns, not significant.
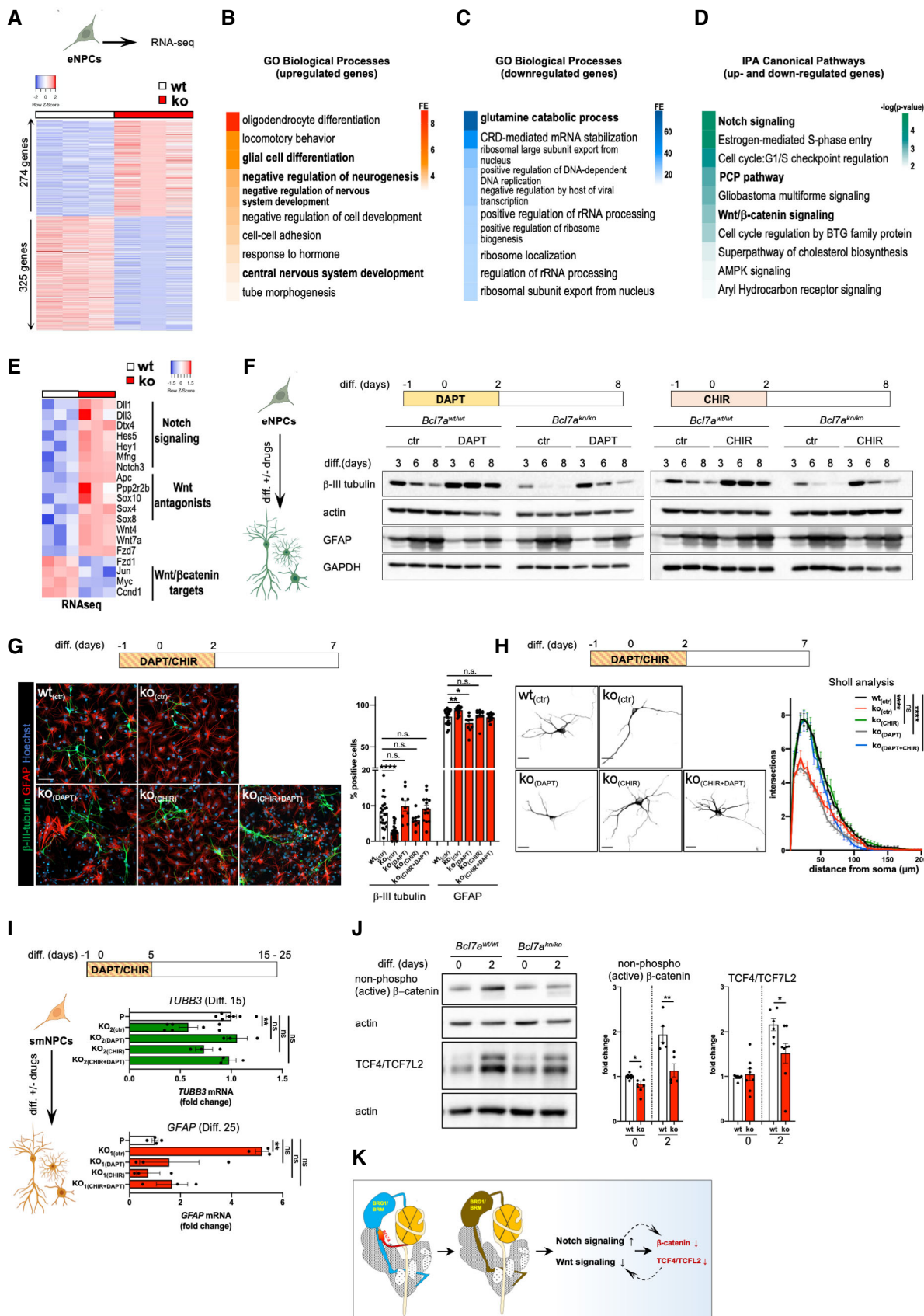
Source data are available online for this figure.

Figure 5.

Notch3) in BCL7A KO compared to wt eNPCs (Figs 5E and EV5A). We also observed that 5 Wnt antagonists (i.e., *Apc, Ppp2r2b, Sox10, Sox4, Sox8*) were upregulated and 3 Wnt/β catenin targets (i.e., *Jun, Myc*, and *Ccnd1*) were downregulated in BCL7A KO cells, indicating an overall diminished Wnt/β-catenin signaling (Figs 5E and EV5B). Thus, our analyses imply a functional link between BCL7A expression and Notch/Wnt signaling cascades, as previously proposed in invertebrates (Haussmann *et al*, 2008; Uehara *et al*, 2015). The differential regulation of some of these genes in Notch and Wnt signaling pathways correlated with a reduced SMARCA4/BRG1 binding at target regions due to BCL7A loss in both proliferating murine eNPCs and human smNPCs (Fig EV5C and D). These data suggest that BCL7A deficiency alters the transcriptional outcomes causally linked to the SWI/SNF/BAF complex activity. Importantly, our findings indicate that BCL7A has a dual role in replicating NPCs, since it suppresses Notch signaling and acts as a positive regulator of the Wnt/β-catenin pathway potentially via transcriptional repression of Wnt signaling inhibitors.

To explore the functional implications of altered Notch pathway, we used the γ-secretase inhibitor DAPT, a small chemical compound that, by suppressing the proteolysis of the Notch receptor, inhibits the Notch signaling cascade (Geling *et al*, 2002). We treated wt and BCL7A KO eNPCs with DAPT (1 μM) or DMSO (control condition) for an initial 24 h in proliferation medium. Thereafter, cells were switched to differentiation medium and treatment continued for an additional 48 h. Afterward, cells were further differentiated under DAPT- and DMSO-free conditions for another 1–6 days and collected at the indicated time points (Fig 5F). In line with our hypothesis, we found that Notch inhibition resulted in an increased expression of β-III tubulin during the course of differentiation (Fig 5F). This positive effect on neurogenesis was further accompanied by a reduction of the fraction of GFAP-positive cells (Fig 5F). Thus, inhibition of Notch signaling is sufficient to ameliorate the neurogenesis defect and skewing toward gliogenesis as seen in spontaneously differentiated BCL7A KO eNPCs. To further investigate the mechanistic contribution of Wnt signaling to NPC differentiation, we exposed eNPCs to the GSK3 inhibitor/Wnt activator CHIR99021 (3 μM) for 24 h before and 48 h during differentiation conditions. We collected cells as described above and performed immunoblots. We found that CHIR99021 exposure increased β-III tubulin levels in BCL7A KO cells compared to untreated cells (Fig 5F). Additional immunocytochemical analyses showed that both DAPT and CHIR99021 ameliorated the neuronal differentiation defects of BCL7A KO eNPCs, since it increased the number of β-III tubulin-positive cells (Fig 5G). Furthermore, both Notch inhibition and Wnt signaling activation reduced the percentage of GFAP-positive cells indicating a reduction of gliogenesis (Fig 5G). We next performed Sholl analysis of untreated and treated eNPC exposed to differentiation media and showed that CHIR99021 treatment completely rescued the defects in neurite arborization due to BCL7A loss (Fig 5H). Conversely, DAPT inhibition of Notch signaling did not promote dendritic branching in BCL7A KO cells (Fig 5H). Of note, DAPT and CHIR99021 treatment also resulted in a higher percentage of β-III tubulin cells along with a reduction of GFAP-positive astrocytes in spontaneously differentiated wt eNPCs (Fig EV5E), while an increase in neurite complexity was again only seen upon Wnt signaling stimulation (Fig EV5F). Similar to our observations in mouse eNPCs, DAPT, and CHIR99021 treatment

during the first 2 and 5 days of differentiation, respectively, led to increased *TUBB3* and decreased *GFAP* mRNA levels in spontaneously differentiated BCL7A KO smNPCs (Fig 5I). Differentiated control cells did not show major changes in *TUBB3* mRNA levels but a significant reduction of *GFAP* expression following DAPT and CHIR99021 treatment (Fig EV5G). These data suggest that BCL7A contributes to neural commitment and differentiation through inhibition of Notch signaling and enhanced Wnt signaling.

To further strengthen the evidence linking BCL7A loss to defective Wnt activity, we next performed immunoblot analysis for dephosphorylated (active) β-catenin along with TCF4/TCF7L2 as one of the key transcription factors regulating Wnt signaling (Paridaen & Huttner, 2014; Fig EV5H). Since canonical Wnt/β-catenin signaling has been shown to be particularly relevant during the early stages of neuronal differentiation (Barker *et al*, 2001; Zechner *et al*, 2003; Lie *et al*, 2005; Heppt *et al*, 2020), we used proliferating eNPCs together with cells that were cultured in differentiation medium for 48 h. We found that proliferating BCL7A KO eNPCs showed reduced non-phospho (active) β-catenin levels compared to wt cells (Fig 5J). Upon differentiation, wt eNPCs showed a strong upregulation of active β-catenin and TCF4/TCF7L2 expression, whereas BCL7A-deficient eNPCs displayed a reduced Wnt signaling (Fig 5J). Treatment with the Wnt signaling activator CHIR99021 restored the levels of non-phospho (active) β-catenin and TCF4/TCF7L2 in proliferating and differentiating BCL7A KO NPCs (Fig EV5H–J). Together, these data indicate that BCL7A-containing SWI/SNF/BAF complex is an upstream regulator of Wnt signaling, since BCL7A deficiency negatively influence β-catenin and TCF4/TCF7L2 expression levels (Fig 5K).

BCL7A-dependent regulation of Wnt signaling potentiates mitochondrial OXPHOS to efficiently support NPC differentiation toward neurons

GO analysis of our ChIP- and RNA-seq data sets predicted aberrant metabolic processes (e.g., cellular nitrogen compound and glutamine catabolism, cholesterol biosynthesis and AMPK signaling) in BCL7A KO eNPCs and smNPCs (Figs 2O, and 5C and D). Thus, we reasoned that BCL7A-containing SWI/SNF/BAF complexes may take part in the fine tuning of metabolism during cell lineage commitment and/or differentiation. To explore this hypothesis, we started off with an RNA-seq analysis on parental and BCL7A KO iPSCs, which revealed 368 genes that were commonly dysregulated ($P < 0.1$, log2 FC ≥ 0.4) in both BCL7A KO clones. Subsequent IPA on downregulated genes predicted mitochondrial dysfunction and oxidative phosphorylation among the top 10 overrepresented pathways while Glycolysis I and Wnt/β-catenin signaling were identified following IPA of upregulated genes (Appendix Fig S3A and B). We next ran conventional Seahorse experiments to assess mitochondrial respiration, however we did not detect major changes in OCR between parental and BCL7A KO iPSCs (Appendix Fig S3C). Yet, there was an evident increase in glycolysis as measured via the extracellular acidification rate (ECAR; Appendix Fig S3D). Based on these data, it seems that BCL7A deficiency may cause subtle mitochondrial defects already in proliferating stem cells.

Since efficient mitochondrial OXPHOS is essential during neuronal differentiation (Khacho *et al*, 2016; Beckervordersandforth *et al*, 2017; Lorenz *et al*, 2017; Adusumilli *et al*, 2021; Inak *et al*,

2021; Russo *et al*, 2021), we asked whether BCL7A influences NPC biology by altering the expression of genes involved in mitochondrial function. To do so, we performed RNA-seq on wt and BCL7A KO eNPCs that had been differentiated for 48 h and found 1,175 DEGs in BCL7A-deficient cells (Fig 6A). GO analysis of the downregulated genes indicated impaired glutamate catabolism among the most overrepresented biological process (Appendix Fig S3E), similar to our observations in proliferating BCL7A KO eNPCs (Fig 5C). However, pharmacological manipulation of the glutamine/glutamate pathway with the potent glutaminase GLS1 inhibitor BPTES did not significantly alter Seahorse profiles of proliferating eNPCs and smNPCs (Appendix Fig S3F–H). Since altered glutamate metabolism cannot explain the observed Seahorse profiles, we next carried out IPA of all altered genes and found mitochondrial dysfunction and aberrant OXPHOS among the top 10 significantly enriched canonical pathways (Fig 6B). When we overlayed our NGS data with MitoCarta 3.0 (Rath *et al*, 2021), we found that 73 genes encoding mitochondrial proteins were significantly down-regulated, while 16 genes were upregulated (Fig 6C). Through a more in-depth comparative analysis of SMARCA4/BRG1 ChIP-seq data and DEGs, we further found that ~35% (362 out of 1,051) of mitochondrial genes are bound by SMARCA4/BRG1 in proliferating eNPCs (Fig 6D$_1$). The differential regulation of some of these genes (e.g., *Ndufc2*, *Cox6c*, *Gls*) correlated with reduced SMARCA4/BRG1 binding to targeted loci in BCL7A KO eNPCs and smNPCs (Fig 6D$_2$). Moreover, reduced SMARCA4/BRG1 enrichment was observed at genes (e.g., *Pparg/PPARG*, *Ppargc1a/PPARGC1A, and Nrf1/NRF1*) encoding for transcription factors regulating mitochondrial biogenesis (Fig 6D$_3$ and D$_4$), which could imply that aberrant SMARCA/BRG1 deposition may transcriptionally influence mitochondrial activity. When we performed OCR measurements, maximal respiration was decreased in proliferating BCL7A KO eNPCs and smNPCs compared to controls (Fig 6E and F), although the detected OCR defects were not accompanied by obvious morphological alterations of the mitochondrial network (Appendix Fig S3I and J). To detect mitochondrial changes in the hippocampus of conditional BCL7A KO mice, we employed a proximity ligation assay (PLA)-based method that we recently validated to measure mitochondrial complex I and complex IV-containing respiratory supercomplexes (CI*CIV-SCs) as a functional proxy of mitochondrial OXPHOS integrity (Bertan *et al*, 2021). High-resolution confocal microscopy and

subsequent quantification showed a reduction of CI*CIV-SCs in BCL7A KO neurons compared to controls (Fig 6G), further indicating a role of BCL7A in regulating mitochondrial bioenergetics.

Having experimentally confirmed the predicted signatures of mitochondrial dysfunction, we sought to determine how BCL7A regulates mitochondrial function during NPC differentiation. First, we exposed proliferating and differentiating eNPCs to CHIR99021 for 24 or 72 h, respectively. Seahorse experiments showed that CHIR99021 rescued the mitochondrial respiratory defects due to BCL7A KO in both proliferating as well as early differentiated eNPCs (Fig 7A and B). Consistently, CHIR99021 treatment ameliorated OCR defects in BCL7A KO smNPCs compared to controls (Appendix Fig S4A). With this knowledge, we incubated eNPCs with CHIR99021 for 24 h before and 48 h after the cells were exposed to differentiation media, in presence or absence of complex I inhibitor rotenone (Fig 7C). We collected cells at different time points and performed immunoblot analysis for β-III tubulin. We found that rotenone treatment abrogated the rescuing effect of CHIR99021 (Fig 7C), suggesting that Wnt signaling requires functional mitochondria to stimulate neurogenesis. We repeated the experiment, stained additional cultured cells and quantified β-III tubulin- and GFAP-positive cells upon exposure to CHIR99021, in presence or absence of rotenone. Consistent with our immunoblots, rotenone treatment of BCL7A KO cells significantly reduced the number of β-III tubulin-positive neurons upon CHIR99021 treatment (Fig 7D). Moreover, rotenone exposure of BCL7A KO NPCs enhanced the number of GFAP-positive glia cells, despite that these cells were cultured in presence of CHIR99021 (Fig 7D). As revealed by Sholl analysis (Fig 7E), complex I inhibition abrogated the formation of elaborated dendritic arborization in CHIR99021-treated BCL7A KO eNPCs. To further strengthen the relevance of mitochondrial function in NPC differentiation, we next assessed whether stimulation of mitochondrial biogenesis could attenuate the neurogenic defects of BCL7A KO eNPCs. We therefore treated proliferating BCL7A KO eNPCs with pioglitazone, a compound that has been shown to enhance mitochondrial biogenesis by increasing the expression of proliferator-activated receptor (PPAR)-γ coactivator-1α (Bogacka *et al*, 2005). We found that pioglitazone treatment enhanced maximal mitochondrial respiration of BCL7A KO eNPCs in a dosedependent manner (Fig 7F). Additionally, spontaneously differentiated BCL7A KO eNPCs showed a slightly higher percentage of β-III

▶

Figure 6. BCL7A KO impairs mitochondrial bioenergetics.

A   Heatmap of significantly dysregulated genes in BCL7A KO compared to wt eNPCs, which were exposed to differentiation medium for 48 h.

B   IPA of up- and down-regulated genes and relative prediction of the top 10 most significantly overrepresented canonical pathways.

C   Heatmap of significantly dysregulated mitochondrial genes in BCL7A KO vs. wt eNPCs. Cells were exposed for 48 h to differentiation medium before RNAs were extracted.

D   (D$_1$) Genome browser screenshots of SMARCA4/BRG1 ChIP-seq signals in eNPCs (left hand panels) and smNPCs (right hand panels). Peaks show the reduced SMARCA4/BRG1 occupancy at representative mitochondrial genes (i.e., *Ndufc2*, *Cox6c*, *Gls/GLS*) in control and BCL7A KO cells. (D$_2$) Overlap between SMARCA4/BRG1-bound genes, DEGs and mitochondrial genes identified in MitoCarta 3.0. (D$_{3-4}$) Genome browser screenshots of SMARCA4/BRG1 ChIP-seq signals in (D$_3$) eNPCs and (D$_4$) smNPCs. Peaks show the reduced SMARCA4/BRG1 occupancy at transcription factors known to be involved in mitochondrial biogenesis.

E, F   OCR measurements in in control and BCL7A KO (E) eNPCs and (F) smNPCs. On the right, it is reported the maximal respiration following treatment with the mitochondrial uncoupler FCCP ($n = 5$ biological replicates).

G   Proximity ligation assay (PLA) for the OXPHOS subunits NDUFB8 and MTCO1 in adult hippocampal sections from *Bcl7a$^{fl/fl}$*; *Baf53b-Cre$^{tg/wt}$* (ko; $n = 4$) and control littermates (ctr; $n = 4$). Sections were co-stained with TOM20 and NeuN to label mitochondria and neurons, respectively. The total number of PLA dots was normalized to the mitochondrial area (panel on the lower right). Scale bars = 10 μm.

Data information: Data in (E–G) are presented as mean ± SEM. In (E–G), unpaired two-tailed Student's *t* test and one-way ANOVA followed by Bonferroni's *post hoc* test for multiple comparisons was used. *$P < 0.05$, **$P < 0.01$.
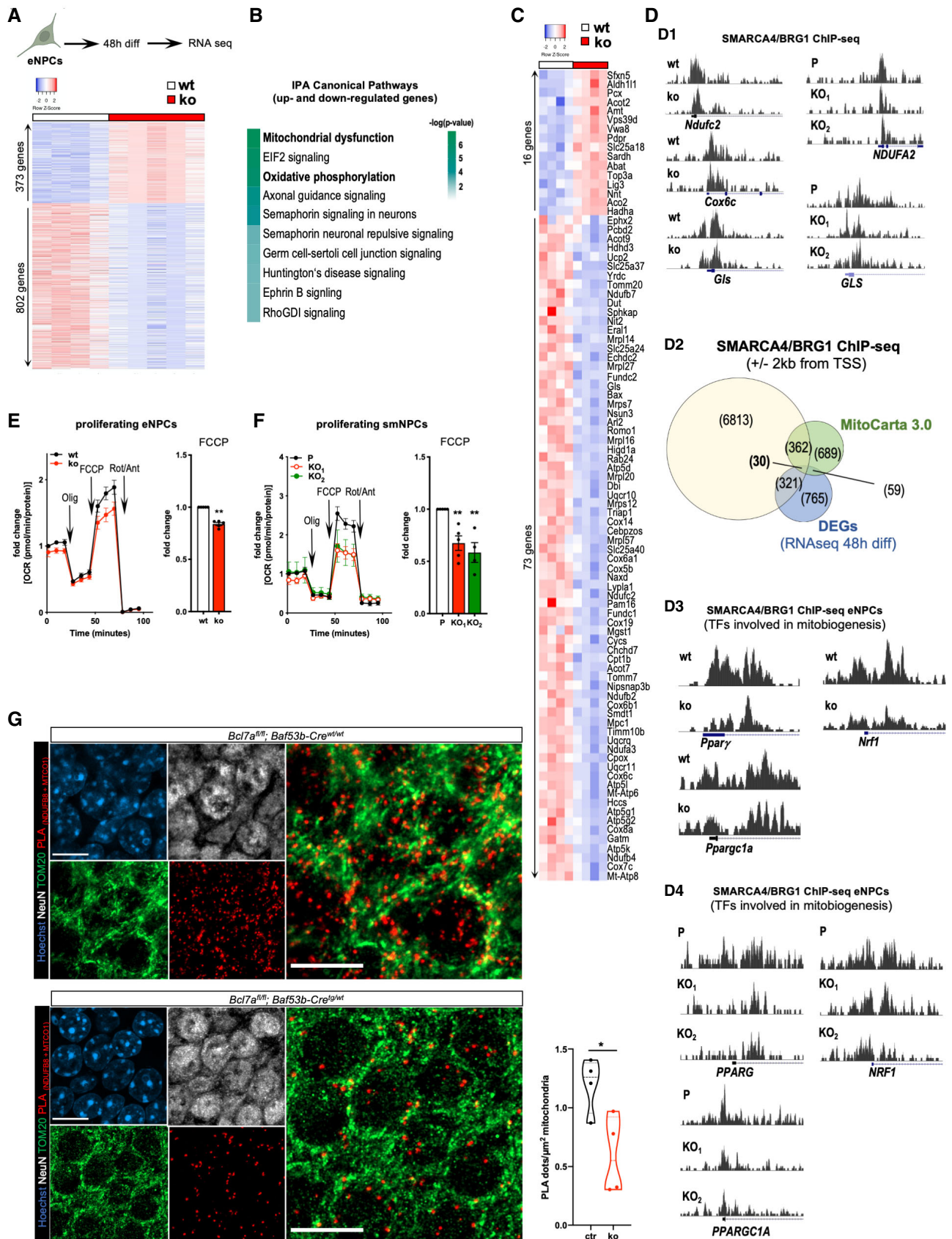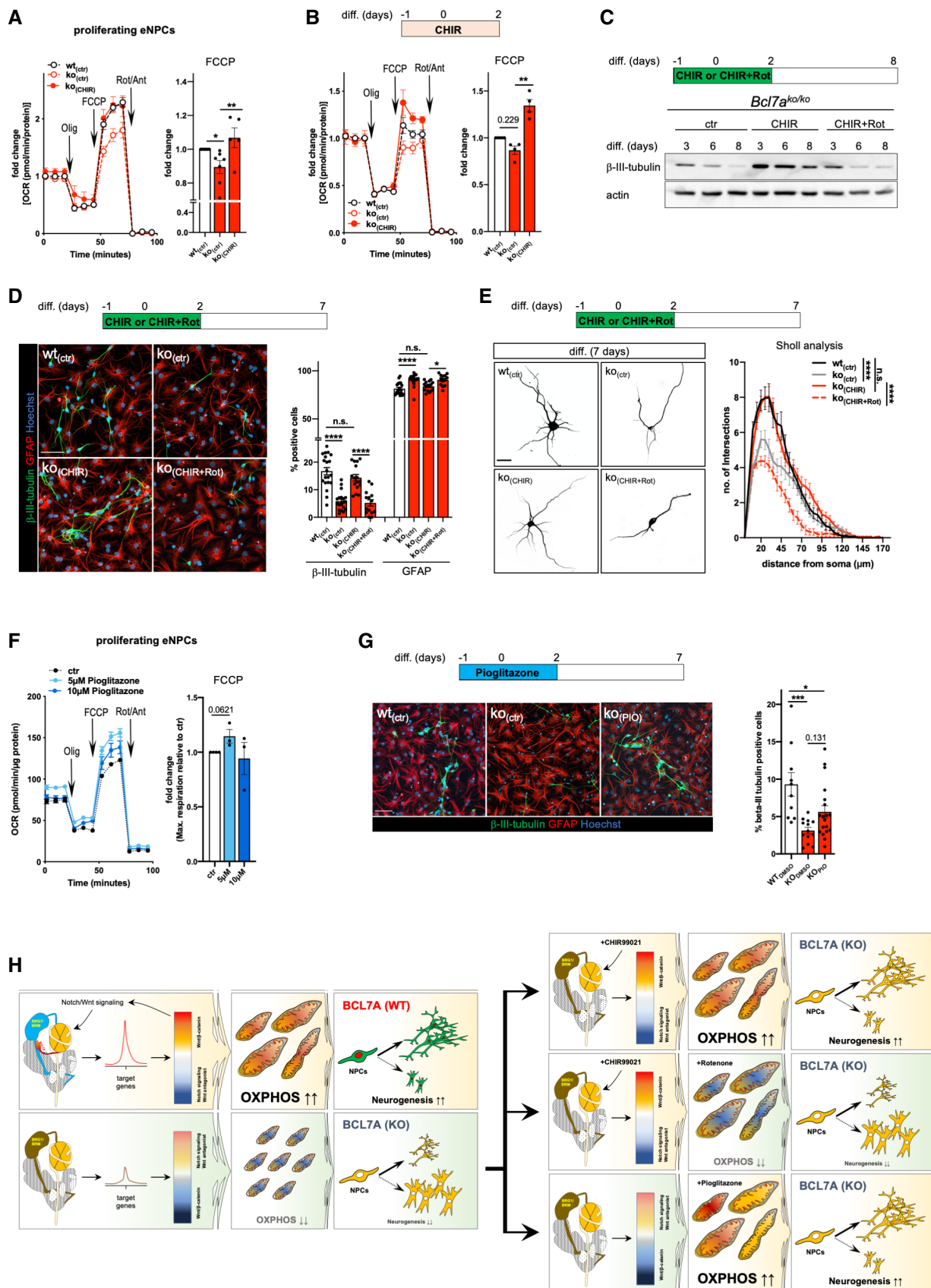
Figure 6.

Figure 7.

Figure 7. Stimulation of Wnt signaling ameliorates OXPHOS and neurogenesis defects of BCL7A KO eNPCs.

A OCR measurements in wt and BCL7A KO eNPCs treated with 3 µM of CHIR99021 or DMSO (as control, ctr) for 24 h. The average maximal respiration upon FCCP treatment is shown on the right ($n = 5$–7 biological replicates).

B OCR measurements in wt and BCL7A KO eNPCs following 48 h of spontaneous differentiation. BCL7A KO eNPCs were treated for 72 h (24 h in proliferation plus 48 h in differentiation medium) with CHIR99021 or DMSO. The average maximal respiration upon FCCP treatment is shown on the right ($n = 4$ biological replicates).

C Immunoblot analysis of differentiated BCL7A KO eNPCs exposed to 3 µM of CHIR99021, in presence or absence of 20 nM of rotenone (rot). Antibodies against β-III tubulin and actin were used.

D Immunofluorescence staining of spontaneously differentiated eNPCs. BCL7A KO eNPCs were treated for 72 h (i.e., 24 h in proliferation plus 48 h in differentiation medium) with 3 µM of CHIR99021, in presence or absence of 20 nM of rotenone. Scale bar = 50 µm. Statistics are shown on the right ($n = 3$–6 technical replicates from three independent experiments).

E Sholl analysis of β-III tubulin-positive immature neurons following 7 days of spontaneous differentiation. BCL7A KO eNPCs were exposed to 3 µM CHIR99021, in presence or absence of 20 nM of rotenone ($n = 3$ biological replicates). Scale bar = 20 µm.

F Representative OCR measurements in BCL7A KO eNPCs treated with 5 and 10 µM of pioglitazone or DMSO (as control, ctr) for 24 h. The average maximal respiration upon FCCP treatment is shown on the right ($n = 3$ biological replicates).

G Immunofluorescence staining of spontaneously differentiated eNPCs. BCL7A KO eNPCs were treated for 72 h (i.e., 24 h in proliferation plus 48 h in differentiation medium) with 5 µM of pioglitazone. The percentage of β-III-tubulin-positive cells is shown on the right ($n = 3$–8 technical replicates from two independent experiments). Scale bar = 50 µm.

H Schematic representation of our main findings. In differentiating NPCs, BCL7A expression is required for the correct regulation of Notch and Wnt pathways. Loss of BCL7A compromises mitochondrial bioenergetics and skews NPC differentiation toward glia. Pharmacological activation of Wnt/β-catenin by CHIR99021 potentiates mitochondrial respiration and partially rescues the neurogenic defects of BCL7A KO NPCs. Conversely, rotenone-mediated complex I deficiency abrogates the positive neurogenetic effect of CHIR99021. Stimulation of mitochondrial biogenesis by pioglitazone partially compensates for BCL7A deficiency during NPC differentiation.

Data information: In (A), (B), (D), (F), and (G) one-way ANOVA followed by Bonferroni's *post hoc* test for multiple comparisons was used, while in (E) two-way ANOVA, with repeated measures where appropriate, with Tukey's multiple comparisons test was done. $*P < 0.05$, $**P < 0.01$, $***P < 0.001$, $****P < 0.0001$.
Source data are available online for this figure.

---

tubulin-positive cells following 72 h of pioglitazone treatment (Fig 7G). Together, these data strongly imply that through BCL7A-containing SWI/SNF/BAF complex, Wnt signaling transcriptionally stimulates mitochondrial bioenergetics to support NPC differentiation toward neurons (Fig 7H).

Discussion

We herein report that the SWI/SNF/BAF complex contributes to neurogenesis by potentiating Wnt signaling and mitochondrial bioenergetics in NPCs. We identify the SWI/SNF/BAF complex subunit BCL7A as a novel molecular determinant modulating NPC fate and neuronal differentiation in multiple *in vitro* and *in vivo* experimental models. Our comprehensive study fills several gaps of knowledge in the field. Consistent with previous evidence in tumorigenic B-cell lines expressing nonfunctional truncated BCL7A variants (Balinas-Gavira *et al*, 2020), we report that BCL7A loss does not impact the integrity of the residual SWI/SNF/BAF complex in mouse and human NPCs. At the functional level, our experimental work indicates that BCL7A stimulates the genome-wide binding of BRG1 to selected promoters and enhancer regions in NPCs. However, as a note of caution, we also highlight that BCL7A acts on SWI/SNF/BAF complex deposition in a biological context-dependent manner, since BCL7A KO can compromise BRM binding in tumorigenic HAP1 cells. Taking into consideration all these aspects, we propose that BCL7A is a SWI/SNF/BAF complex subunit that evolved in metazoans to assist the activity of the ATP-dependent chromatin remodeler, possibly through its binding to nucleosomal H2A/H2B as previously suggested (Mashtalir *et al*, 2018, 2020). The modulatory effect of BLC7A deficiency is less marked compared to disease-causing *SMARCB1/BAF47* mutations, which significantly reduce the ATPase activity and consequent nucleosome remodeling (Valencia *et al*, 2019). Thus, in the biological context (NPC differentiation) thoroughly investigated in this

study, BCL7A KO does not displace BRG1 to its genomic targets as it occurs in cells lacking other SWI/SNF/BAF complex subunits, such as BAF170, BAF155, or BAF47 (Narayanan *et al*, 2015; Wang *et al*, 2017).

Seminal investigations in invertebrates and in higher organisms have postulated that Polycomb group (PcG) members and chromatin remodelers of the Trithorax group have an evolutionarily conserved role in the epigenetic regulation of chromatin structure and accessibility, with their recruitment and activity influencing transcriptional permissibility according to the biological context (e.g., differentiation programs, cell proliferation; Ringrose & Paro, 2004; Ronan *et al*, 2013; Zhang *et al*, 2015; Kadoch *et al*, 2016; Schuettengruber *et al*, 2017; Bracken *et al*, 2019). Because this aspect is relevant in biomedicine (Helming *et al*, 2014; Hohmann & Vakoc, 2014; Morgan & Shilatifard, 2015; Kadoch *et al*, 2016; Alfert *et al*, 2019; Bracken *et al*, 2019; Valencia & Kadoch, 2019), we designed ChIP-seq and bioinformatic analyses that addresses the consequence of BCL7A deficiency in H3K27me3 profiles. Based on our line of experimental evidence, it appears that reduced BRG1 occupancy does not directly correlate with major changes in the deposition of the silent histone mark H3K27me3 at promoter and enhancer regions. At least in proliferating mouse-derived eNPCs and human smNPCs, it is conceivable to think that BCL7A loss does not influence the antagonistic role of BRG1 to PRC2 function and eventually occupancy, as previously described for other aberrant SWI/SNF/BAF complexes in tumorigenic cells (Kim *et al*, 2015; Kadoch *et al*, 2016, 2017; McBride *et al*, 2018). Thus, our data describe the physiological contribution of BCL7A in modulating, but not altering, BRG1 genome targeting that is associated with the transcriptional regulation of stemness and neurogenesis.

We next sought to identify the biological consequences of BCL7A loss. Based on our pathway analyses (i.e., ClueGO and IPA) of ChIP-seq and RNA-seq data, BCL7A KO interferes with NPC fate, including their maintenance and commitment toward neurogenesis and neuronal differentiation. To confirm these predictions, we

established a series of complementary investigations using cultured cells and transgenic mice. As a first step, we demonstrate that BCL7A deficiency skews differentiation of mouse-derived and iPSC-derived NPCs toward gliogenesis. We reveal that BLC7A loss undermines the proper formation of the dendritic branching in immature neurons undergoing differentiation. Next, we correlate our *in vitro* findings with *in vivo* data obtained by using adult transgenic mice. In adulthood, we provide evidence that *Nestin-Cre*-driven deletion of *Bcl7a* considerably reduces EdU/DCX-double positive cells, whereas it increases the number of glial cells. Remarkably, BCL7A loss interferes with NPC differentiation, with newly developed neurons that exhibit shorter neural projections and less sophisticated dendritic branching compared to controls. While BCL7A KO in progenitor cells disturbs the integration of newly differentiated neurons into existing neural circuitry, a milder effect is observed when BCL7A deficiency occurs post mitotically. Prior evidence in our laboratory indicates that partial deletion of *Bcl7a* in postmitotic cells does not elicit cognitive dysfunction in adult animals (Wischhof *et al*, 2017). Here, we report that full *Bcl7a* KO during embryogenesis primes animals to behavioral abnormalities, including hippocampus-dependent contextual memory function. Thus, our *in vivo* findings reveal a critical contribution of BCL7A in NPC differentiation as well as in postmitotic neuronal maintenance. Although we cannot completely dismiss the possibility that its paralogs (i.e., BCL7B plus BLC7C) may compensate for BCL7A loss, our additional evidence in *Bcl7b*[KO/KO] animals further implies a unique role of BCL7A in mammalian brain as previously proposed (Wischhof *et al*, 2017). As a major limitation of our study, we were not able to link BCL7A-dependent adult neurogenesis to animal behavior, since we cannot rule out an embryonic developmental signature that contributes to the observed phenotypes. In this respect, it would be interesting in the future to assess cognitive performance during aging when BCL7A expression is manipulated in a tissue-specific manner or in a subset of precursor cell population. Having that said, our transgenic *Bcl7a* and *BCL7b* KO mice might represent valuable models to study neurodevelopmental processes associated with SWI/SNF/BAF complex inhibition. At least in the aforementioned biological context, genetic inhibition of *Bcl7a* may represent an alternative experimental approach to efficiently modulate the activity of the SWI/SNF/BAF complex without considerably altering the integrity of the assembly.

Our study provides insights into BCL7A mechanisms of action that influence NPC fate and neurogenesis. We suggest that BCL7A KO enhances Notch signaling and inhibits the Wnt pathway, ultimately skewing NPC commitment toward gliogenesis. In this regard, we demonstrate that pharmacological inhibition of Notch and activation of Wnt signaling cascades stimulates NPC differentiation, with the potent glycogen synthase kinase 3 (GSK-3) inhibitor promoting Wnt signaling cascade and consequent development of complex dendritic branches in immature neurons. We postulate that both Notch and Wnt signaling pathways are required for NPC commitment, although Wnt signaling cascade primarily contributes to the full differentiation of immature neurons in a BCL7A-dependent manner. Consistent with the previously reported epistatic effect of BCL-7 on Wnt signaling in invertebrates (Haussmann *et al*, 2008; Uehara *et al*, 2015), we clearly show that BCL7A KO is an upstream regulator of Wnt signaling, since it controls β-catenin and TCF4/TCF7L2 expression levels. Thus, we conclusively elucidate

the mechanistic contribution of the BCL7A-containing SWI/SNF/BAF complex in integrating and translating multiple signals (e.g., Notch and Wnt) into transcriptional profiles that support neuronal morphogenesis (e.g., dendritic arborization). In this regard, we demonstrate that BCL7A expression is required for the efficient regulation of mitochondrial bioenergetics underlying neurogenesis. In line with previous observations (Yoon *et al*, 2010; Costa *et al*, 2019), our correlative analysis between SMARCA4/BRG1 ChIP-seq data and DEGs suggests a model in which Wnt signaling induces the recruitment of BCL7A-containing SWI/SNF/BAF complex to transcriptionally regulate Wnt targets as well as genes involved in mitochondrial biogenesis and bioenergetics, the latter being essential to provide an adequate energy supply for the highly demanding differentiation programs that establish neuronal morphology and activity. In a broader context, these data contribute to address a long-lasting question in the field and describe how the metabolic switch occurs during NPC differentiation in neurons and/or glia.

In summary, our study goes beyond the physiological characterization of a SWI/SNF/BAF complex subunit. We conclusively demonstrate that BCL7A expression during neurogenesis is the key modulator for the proper coordination of signaling cascades (e.g., Notch and Wnt signals) that define the expression of hundreds of genes involved in mitochondrial OXPHOS and necessary for neuronal morphogenesis. Moreover, our investigation mechanistically elucidates the link between SWI/SNF/BAF complex activity, mitochondrial bioenergetics, cell fate specification, and animal behavioral performance. Apart from the unique functional properties of the SWI/SNF/BAF complexes during neurodevelopment, we envision that these chromatin remodelers may uninterruptedly take part in the maintenance and remodeling of the central nervous system as a "translator" of extrinsic and intrinsic cues throughout the whole lifetime of an organism, possibly also during pathological processes.

Materials and Methods

Antibodies

Mouse anti-actin (MAB1501, Sigma), rabbit anti-BAF47 (8745, Cell Signaling), rabbit anti-BAF53A (NB100-61628, Novus Biologicals), rabbit anti-BAF53B (ab140642, Abcam), rabbit anti-BAF60A (OAAN04064, Aviva Systems Biology), rabbit anti-BAF60C (62265, Cell Signaling), rabbit anti-BAF155 (11956, Cell Signaling), rabbit anti-BAF170 (12760, Cell Signaling), rabbit anti-BCL7A (HPA019762, Sigma), rabbit anti-BCL7B (11751-1-AP, Proteintech), rabbit anti-BRG1 (ab110641, Abcam), mouse anti-BRG1 (MA5-31550, Invitrogen), rabbit anti-BRM (11966, Cell Signaling and ab15597, Abcam), rabbit anti-α 1 Fetoprotein (ab284388, Abcam), rabbit anti-cFos (226003, Synaptic Systems), chicken anti-DCX (ab153668, Abcam), rabbit anti-GAPDH (2118, Cell Signaling), mouse anti-GFAP (3670, Cell Signaling), chicken anti-GFAP (ab4674, Abcam), mouse anti-total OXPHOS (ab110413, Abcam), mouse anti-MTCO1 (ab14705, Abcam), rabbit anti-NDUFB8 (14794-1-AP, Proteintech), mouse anti-Nestin (MAB353, Merck), mouse anti-Nestin (MAB1259, R&D Systems), chicken anti-NeuN (ABN91, Millipore), rabbit anti-NeuN (Abcam, ab177487), rabbit anti-non-phospho (active) β-catenin (8814, Cell Signaling), rabbit anti-S100β

(ab52642, Abcam), mouse anti-smooth muscle actin (ab7817, Abcam), rabbit anti-SOX2 (ab92494, Abcam), rabbit anti-SOX10 (ab155279, Abcam), rabbit anti-TCF4/TCF7L2 (2569, Cell Signaling), mouse anti-TOM20 (sc-17764, Santa Cruz), rabbit anti-TOM20 (11802-1-AP, Proteintech), mouse anti-α tubulin (T6074, Sigma), mouse anti-β-III tubulin (G7121, Promega), rabbit anti-β-III tubulin (T3952, Sigma); appropriate Alexa Fluor-conjugated secondary antibodies were obtained from Invitrogen while horseradish peroxidase-conjugated secondary antibodies were purchased from Promega and Invitrogen.

Behavioral tests

Male and female mice at the age of 3–4 months were used for behavioral assessments. Prior to testing, animals were handled daily for 7 days. To minimize effects of previous testing on subsequent behaviors, behavioral tests were performed in a specific order where less stressful tests preceded the more stressful ones. *Open field*. Spontaneous locomotor activity was assessed in open field boxes (27 × 27 × 27 cm) in an evenly lit room. Each mouse was placed individually in the center of the box and its behavior was recorded for 20 min. The distance moved was analyzed using the EthoVision tracking system (Noldus, The Netherlands). *Rotarod*. Motor coordination was assessed using a rotarod system (TSE Systems, Bad Homburg, Germany). Mice were trained to remain on the rod, which rotated with accelerating speed (4–40 rpm) for three consecutive days with three daily sessions and a maximum session duration of 5 min. A 30-min break was given between individual training sessions. When a mouse fell from the rod, infrared light beams at the bottom of the chamber were interrupted allowing to measure the fall latency (s). *Y-maze spontaneous alternation task*. A Y-maze apparatus was used to assess working memory function. It consisted of three equilateral arms made of opaque plastic and was placed in a well-lit room with several external cues. Mice were put into the center of the maze and were then allowed to freely explore it for 6 min. The number and sequence of arms entered was scored by an observer blind to the genotype of the mice. The total number of arm entries was used as activity index and mice with less than a total of 10 arm visits were excluded from the analysis. The percentage of spontaneous alternations was calculated by the number of consecutive entries into three different arms divided by the number of total possible alternations (i.e., the number of arms entered minus 2) and multiplied by 100. *Barnes maze*. The Barnes maze consisted of a circular platform (100 cm in diameter) with 18 holes evenly spaced around the periphery, that was placed in a brightly lit room with several spatial clues. One of the holes (target hole) was connected to an escape box. At 24 h before the first training day, a 5 min-habituation session was performed during which mice were allowed to freely explore the maze and the escape box. Thereafter, animals were trained to locate the escape box for four consecutive days with four training trials per day and a maximum trial duration of 180 s. During the entire training period, the escape box remained at a fixed position while the animals' starting position was semi-randomized so that each trial started from a different quadrant. Long-term memory was then assessed in a 1 min probe trial (with the escape box removed) 72 h days after the last training session. During training sessions, the latency to find the escape box as well as movement velocity and distance were analyzed via a video tracking system (EthoVision). Memory performance during the probe trial was assessed via the time spent in the target (i.e., area where the escape box was previously positioned) compared to nontarget quadrants. *Contextual fear conditioning*. Fear conditioning was conducted in transparent plastic boxes (21.5 × 20 × 25 cm) with stainless-steel grid floors connected to an aversive stimulator (Med Associates). For fear conditioning, mice were placed individually into the chamber and allowed to habituate for 2 min. Thereafter, three-foot shocks (0.75 mA, 2 s) with an inter-shock interval of 60 s were delivered. Animals were removed from the boxes 60 s after the last shock and placed back into their home cages. Fear memory retrieval was than assessed 24 h afterward by re-introducing the mice into the chamber for 5 min without the presentation of foot shocks. During fear conditioning and fear memory retrieval, animals were video recorded and the time spent freezing was analyzed and used as an index for contextual fear memory.

Cell culture

Embryonic neural progenitor cells (eNPCs) were isolated from the cortex of E12.5-E13.5 $Bcl7a^{wt/wt}$ and $Bcl7a^{ko/ko}$ mouse embryos. Embryos were prepped individually to maintain genetic identity of subsequent cultures. Following dissection, cortices were placed in HBSS on ice and dissociated with 0.05% trypsin (Gibco) and DNase I (Roche) for 40 min in a water bath at 37°C. The reaction was stopped by the addition of growth factor-free NPC proliferation medium (NeuroCult, StemCell) supplemented with 10% FBS (Gibco). Cells were dissociated by pipetting and the cell suspension was then filtered through a 70 μm cell strainer. Following centrifugation, the cell pellet was resuspended in NPC proliferation medium supplemented with EGF (20 ng/ml, Invitrogen), FGF (20 ng/ml, Invitrogen), primocin (InVivoGen), and plasmocin (InVivoGen). Cells were then seeded onto laminin (Sigma)-coated cell culture dishes. One to two days after plating, medium was replaced with fresh NPC prolifertaion medium, supplemented with half the amount of growth factors (10 ng/ml each) and without primocin and plasmocin. The same media conditions were used for subsequent NPC culture and cells were split when reaching around 80% confluency using accutase. For differentiation experiments, eNPCs (passage 2 to 5) were seeded either onto laminin-coated 6-well plates (300,000 cells/well), Matrigel-coated glass cover slips in 12-well plates (150,000 cells/well), or Seahorse microplates (60,000 cells/well) in proliferation medium. After 24–48 h (i.e., differentiation day 0), medium was replaced by NPC differentiation medium (NeuroCult, StemCell) with one complete medium change on differentiation day 2 and half medium changes every 2–3 days thereafter. At the indicated time points, differentiated cells were collected or fixed in 4% PFA as described below. For experiments involving drug treatments, cells were first plated in proliferation medium as mentioned above, and, after 24 h, NPC proliferation medium containing 1 μM of DAPT (Tocris), 3 μM of CHIR99021 (Miltenyi Biotec, Germany), and/or 20 nM of rotenone (Sigma) was added. Pioglitazone (Sigma) was used at a concentration of 5 and 10 μM. All drugs were dissolved in DMSO. On the next day (i.e., 24 h after the start of drug treatment), the medium was changed to NPC differentiation medium containing the respective drugs at the same concentration. Drug treatment continued for an additional 48 h (i.e., until differentiation day 2) after which cells were further differentiated in normal NPC differentiation medium for the indicated time points.

Primary cortical neurons were isolated from $Bcl7a^{wt/wt}$ and $Bcl7a^{ko/ko}$ mouse embryos at E14.5 as described previously (Bano et al, 2010; Ziviani et al, 2011). Embryos were prepped individually to maintain genetic identity of subsequent cultures. Briefly, dissociated neurons were plated onto poly-lysine coated glass coverslips (25 mm in diameter) and maintained in Neurobasal medium (Invitrogen), supplemented with 2 mM of GlutaMax, 2% B27 supplement (Gibco), and 1% penicillin–streptomycin. Half-medium changes were done every 3 days until cells were used for Ca^{2+} measurements at DIV10.

Human BCL7A KO iPSCs were generated by Horizon Discovery. iPSCs were cultured under feeder-free conditions in StemMACs iPS-Brew (Miltenyi Biotec) on vitronectin-coated 6-well plates. The medium was changed daily and PBS-EDTA was used for splitting. For undirected differentiation experiments, iPSCs were grown in StemMACs iPS-Brew in noncoated 6-well plates for 5 days to allow the formation of embryoid bodies (EBs). Thereafter, EBs were transferred onto gelatin-coated plates with or without coverslips and the medium was switched to serum-containing MEF-medium (DMEM, 10% FBS, 1% nonessential amino acids, 2 mM of L-glutamine, 0.1 mM of β-mercaptoethanol), which induces spontaneous differentiation. The medium was replaced every other day. After 7–28 days in differentiation medium, cells were either fixed in 4% PFA for immunocytochemical analysis or collected for biochemistry.

iPSC-derived smNPCs were generated as described previously (Reinhardt et al, 2013). Briefly, iPSC colonies were dissociated using accutase, collected by centrifugation and resuspended in neural induction medium DMEM-F12/Neurobasal (Invitrogen), 1:200 N2 supplement (Invitrogen), 1:100 B27 supplement without vitamin A (Invitrogen), 2 mM of GlutaMax, supplemented with 10 μM of ROCK inhibitor (Tocris), 10 μM of SB-431542, 1 μM of dorsomorphin, 0.5 μM of purmorphamine, and 3 μM CHIR99021. Cells were transferred onto nonadherent plates and left undisturbed for 3 days. Thereafter, medium was replaced with neural induction medium lacking ROCK inhibitor. On day 4–5, SB-431542 and dorsomorphin were withdrawn and 150 μM of ascorbic acid were added to the medium. The same medium composition was then used for all subsequent smNPC maintenance. On day six, embryoid bodies were triturated via pipetting and plated into Matrigel-coated 12-well plates. Cells were then spilt at a 1:5 to 1:10 ratio using accutase. After 5–6 splits, cultures were free of contaminating non-smNPCs (less than 1%). All smNPC differentiation experiments were conducted between passage 9 and 13. For undirected differentiation, smNPCs were seeded onto Matrigel-coated 6-well plates (200,000 cells/well), glass coverslips in 12-well plates (100,000 cells/well) or Seahorse microplates (50,000 cells/well) in smNPC maintenance medium. After 24–48 h, medium was changed to smNPC differentiation medium DMEM-F12/Neurobasal (Invitrogen), 1:200 N2 supplement (Invitrogen), 1:100 B27 (Invitrogen), 2 mM of GlutaMax, 1% penicillin–streptomycin, freshly supplemented with laminin (1:1,000, Sigma). During the initial week of smNPC differentiation, complete medium changes were performed every 2–3 days, after which only half-medium changes were conducted. At the indicated time points, differentiated smNPCs were collected or fixed in 4% PFA as described below. For experiments involving drug treatments, cells were first plated in smNPC maintenance medium as mentioned above, and, after 24 h, the medium was changed to smNPC differentiation medium containing 1 μM of

DAPT (Tocris) or 3 μM of CHIR99021 (Miltenyi Biotec, Germany). DAPT treatment was maintained for 5 days, while CHIR treatment was for 7 days, after which cells were further differentiated in normal smNPC differentiation medium for the indicated time points. For directed neuronal differentiation, smNPCs were seeded onto Matrigel-coated 6-well plates (200,000 cells/well) and switched to neuronal differentiation medium (Neurobasal (Invitrogen), 1:50 B27 supplement without vitamin A (Invitrogen), 1:100 N2 supplement (Invitrogen), 2 mM of GlutaMax, 20 ng/ml of BDNF (PeproTech), 20 ng/ml of GDNF (PeproTech), 1 μM of cAMP (Sigma), 200 μM of ascorbic acid, 2 μg/ml of laminin) 24–48 h after plating. Medium changes were conducted once per week and cells were differentiated for 25–30 days.

HAP1 cells were purchased from Horizon Discovery Group and cultured in IMDM (Gibco) supplemented with 10% of FBS (Gibco) and 1% of Penicillin/Streptomycin (Gibco).

cFos assay

Quantification of cFos immunoreactivity was done in hippocampal brain sections of mice following exposure to either standard or enriched environmental conditions. The enriched environment consisted of a cage ($39 \times 20 \times 16$ cm^3) equipped with several tunnels, toys, ladders, and houses while the standard cage ($44 \times 13 \times 25$ cm^3) contained only floor bedding. The enriched cage lacked running wheels in order to keep locomotion comparable between the groups. Mice of both genotypes were randomly assigned to two groups and then exposed to either the standard or enriched environment for 90 min. Thereafter, animals were returned to their home cage for another 45–60 min before being sacrificed by transcardial perfusion. Hippocampal brain sections were immunostained for cFos and imaged using an LSM900 confocal microscope (Zeiss) with a 20× objective. Per mouse, cFos$^+$ cells were quantified within the dentate gyrus (DG) of three consecutive hippocampal brain sections using the "find maxima" function in ImageJ. The total number of cFos$^+$ cells was then normalized to the respective area of the hippocampal DG. Imaging and image analysis were done by an experimenter blinded to mouse genotype and treatment conditions.

Chromatin immunoprecipitation sequencing

For chromatin immunoprecipitation sequencing (ChIP-seq) experiments, cells were fixed with formaldehyde, scraped and pelleted by centrifugation. Following two washes with PBS-Igepal (0.5%), cells were snap frozen and stored at -80°C until use. Chromatin from at least two biological replicates was pooled and ChIP-seq assays were performed by Active Motif using antibodies against BRG1 (ab110641, abcam), BRM (ab15597, abcam), or H3K27me3 (AB_2561020, Active Motif). All ChIP-seq experiments were performed using standard normalization by sequencing an input sample, subtracting unspecific and blacklisted peaks as well as advanced spike-in normalization. Bioinformatic analyses was either done by Active Motif or as follow: for data preprocessing, FASTQ files were adaptor-trimmed by TrimGalore (https://github.com/FelixKrueger/TrimGalore) with default parameters and aligned to either hg19 or mm10 genome by Bowtie2 (Langmead & Salzberg, 2012). Trimmed FASTQ files were also aligned to Dm6 genome for later calculation of scaling factors. Calculation of

scaling factors (Ma *et al*, 2018) and aligned BAM files were down-sampled by Picard (https://broadinstitute.github.io/picard/). To identify differential binding regions for BRG1 and H3K27me3, respectively, down-sampled BAM files were transformed into BED format by Bedtools (Quinlan & Hall, 2010). Differential binding regions were then called by diffReps (Shen *et al*, 2013) with a window size of 100 bp for BRG1 and 300 bp for H3K27me3. Putative enhancer regions were defined based on H3K4me1 peaks in mouse NPCs, downloaded from GEO entry GSM2406793 and lifted over to mm10. H3K4me1 peaks in human NPC were obtained after analyzing data from GEO entry GSE16256. Aligned reads in BED format were downloaded from GEO, and H3K4me1 peaks were called by diffReps with a window size of 300 bp using IP samples as treatment and input as control. Integration of differential BRG1 peaks at promoter and putative enhancer regions was done as follows: promoter region was defined as −3,000 to +500 bp around TSS, which was retrieved from the *Homo sapiens* and *Mus musculus* R packages. Differential binding sites between BCL7A KO and control samples were then determined using the diffReps package, which allows the identification of significant differential binding sites without biological replicates using G-test (Shen *et al*, 2013). For differential BRG1 binding inside promoter regions, differential BRG1 peaks were first filtered by log2FoldChange > 1 and then overlapped with promoter regions. For differential BRG1 enrichment at H3K4me1 peaks, differential BRG1 peaks were overlapped with H3K4me1 regions allowing a maximum gap of 200 bp. Data visualization was done using BigWig files for BRG1/H3K27me3 signal, generated by the bamCompare command in deepTools (Ramirez *et al*, 2014) using input signal as control. These BigWig files were then used in profile and heatmap plotting using depptools. For heatmaps showing the signal of BRG1 along with H3K27me3, the input-normalized BigWig files were used as score files, and differential BRG1 regions that reside in promoter/H3K4me1 were used as region file together with command "computeMatrix scale-regions –a 1000 –b 1000 –bs 5". The resultant matrix was fed to plotHeatmap with "––kmeans 4" to produce the heatmap. For BRG1 binding profiles over TSS genome-wide, TSS loci for hg19/mm10 were obtained through Table Bowser on UCSC Genome Browser and then used as region file together with command "computeMatrix reference-point --referencePoint TSS –a 3000 –b 3000 –bs 10." For BRG1-binding profiles over H3K4me1 regions, H3K4me1 peaks analyzed from GEO datasets were used as region file together with command "compute-Matrix scale-regions –a 1000 –b 1000 –m 5000 –bs 10." Gene and pathway enrichment analysis on differential binding sites was performed using the Cytoscape plug-in ClueGO (Bindea *et al*, 2009).

Co-immunoprecipitation

For co-immunoprecipitation (co-IP) experiments on whole cell lysates, cells were washed with cold PBS and scraped in ice-cold nondenaturing lysis buffer (Abcam) supplemented with protease inhibitors. Following 30 min of incubation on a rotator at 4°C, samples were vortexed at maximum speed and centrifuged (10,000 *g* for 10 min at 4°C). The supernatant was collected and protein concentrations were determined via Bradford assay (Sigma). Approximately 300–500 µg of protein from whole cell lysates or nuclear extractions (see below for details on sample preparation) was used for immunoprecipitation with appropriate antibodies overnight at 4°C. On the next day, protein A/G Sepharose® beads

(Abcam) were added for 2 h at 4°C and beads were eluted with Laemmli buffer. Samples were then loaded onto SDS-PAGE and immunoprecipitated samples were visualized via immunoblot or silver staining using the Silver Quest staining kit (Thermo Fisher).

Density sedimentation

Nuclear extracts were loaded on top of 10 ml of 10–30% glycerol gradients containing 25 mM of HEPES pH 7.9, 0.1 mM of EDTA, 12.5 mM of $MgCl_2$, 100 mM of KCl supplemented with 1 mM of DTT, and protease inhibitors. Samples were centrifuged at 100,000 *g* for 16 h at 4°C using a SW41 rotor. Thereafter, 500 µl of fractions were collected manually from the top to the bottom of the gradient. Proteins from 100 µl of each fraction were then concentrated with 10 µl Strataclean beads (Agilent), loaded onto SDS-PAGE gels and visualized via western blotting.

Differential salt extraction

Differential salt extraction was performed as described previously (Nakayama *et al*, 2017). Briefly, cells were collected in elution buffer (50 mM of Tris–HCl pH 7.4, 1 mM of EDTA, 0.1% NP-40 supplemented with protease inhibitors (Roche) and 1 mM of PMSF), incubated on ice for 5 min and centrifuged (1,000 *g*, 5 min, 4°C). The supernatant was collected and the pellet was resuspended in elution buffer containing 150 mM of NaCl, incubated on ice and centrifuged. This process was repeated with increasing salt concentrations (0, 150, 300, 500, and 1,000 mM NaCl) to collected the soluble fractions. Each fraction as well as the remaining cell pellet was then supplemented with 1% SDS and analyzed via western blot.

Extracellular acidification rate (ECAR) measurements

Glycolysis in iPSCs was assessed using the Glycolysis Stress Test (Agilent) and Seahorse XFe24 Analyzer (Agilent). Approximately 48 h prior to the experiment, dissociated iPSCs were seeded onto cell culture microplates (Agilent Seahorse XF24) in culture medium (StemMACS™ iPS-Brew, Miltenyi Biotec) supplemented with 1 µM of ROCK inhibitor (Y-27632, Miltenyi Biotec, Germany). On the next day, fresh culture medium without ROCK inhibitor was added and cells cultured for an additional 24 h. On the day of the experiment, growth media was replaced with Seahorse XF base medium (Agilent), supplemented with 2 mM of glutamine. Cells were then equilibrated for 60 min in a CO_2-free incubator at 37°C before being placed into the Seahorse XFe24 Analyzer. Following three baseline measurements, glucose (10 mM of final concentration), oligomycin (1 µM final concentration) and 2-Deoxy-D-glucose (2-DG, 50 mM of final concentration) were sequentially added. Changes in the extracellular acidification rate (ECAR) were recorded and used to assess glycolytic function. After the assay, cells were collected lysed and sonicated in RIPA buffer. Protein concentrations were then determined via Bradford assay (Sigma) and raw ECAR values normalized to the respective protein content.

Immunocytochemistry

Cells grown on glass coverslips were fixed in 4% PFA, washed with PBS, and incubated in blocking solution (5% normal goat serum,

0.1% Triton X-100 in PBS) for 1 h at room temperature. Primary antibodies, diluted in blocking solution, were added for 4 h at room temperature or overnight at 4°C. Cells were washed in PBST and incubated with secondary antibodies, diluted in PBS with 1% BSA, for 1 h at room temperature. Following three washes in PBST and Hoechst-33342 counterstaining, coverslips were mounted onto microscope slides with DAKO fluorescence mounting medium. Images were taken on an LSM700 or LSM900 confocal microscope (Zeiss) using a 20× or a 63× oil immersion objective. Image processing and analysis was done in ImageJ or CellProfiler (McQuin et al, 2018).

Immunohistochemistry

Adult mice were anesthetized and transcardially perfused with 4% PFA. Brains were removed, postfixed in 4% PFA overnight, and then stored in 30% sucrose solution for 72 h. Brains were frozen and six series of 35–40-μm thick sections were cut on a cryostat (Leica). Free-floating brain sections were blocked and permeabilized with 10% normal goat serum and 0.5% Triton X-100 in PBS for 1 h at room temperature. Thereafter, sections were incubated with primary antibodies (diluted in blocking solution) for 24–72 h at 4°C. Following three washes in PBST, appropriate fluorophore-conjugated secondary antibodies were added for 2 h at room temperature. Sections were then washed in PBST, counterstained with Hoechst-33342, and mounted onto microscope using DAKO fluorescence mounting medium. For immunohistochemistry in P3-P6 old mice, animals were sacrificed via decapitation and brains were immersion fixed in 4% PFA for 48 h. Following dehydration in 30% sucrose solution, 20-μm-thick brain sections were cut on a cryostat, directly mounted onto microscope slides, and stored at −20°C until further use. Immunofluorescence staining was performed as described above while for brightfield microscopy, sections were first quenched with H_2O_2 before blocking and permeabilization. Following incubation with primary antibodies overnight, sections were incubated with biotinylated secondary antibody solution and then treated with avidin-biotin-peroxidase complex (Vector Laboratories). Color reaction was developed using 3,3′-diaminobenzidine kit (Vector Laboratories).

Images were acquired on an epifluorescence or an LSM700, LSM800, or LSM900 confocal microscope (all Zeiss) using a 20× or 63× oil immersion objective. Image processing and analysis was done in ImageJ.

Intracellular Ca^{2+} imaging

Intracellular Ca^{2+} imaging experiments were performed in mouse cortical neurons (DIV 10) as well as in smNPC-derived neuronal cultures grown on glass coverslips. Cells were loaded with 2 μM of the nonratiometric dye Fluo-4 AM (Molecular Probes) for 45 min at 37°C in artificial cerebral-spinal solution (CSS-5: 120 mM of NaCl, 5 mM of KCl, 1.8 mM of $CaCl_2$, 15 mM of glucose, 25 mM of HEPES pH 7.4, supplemented with 10 μM of glycine). Afterward, cells were incubated for an additional 15 min in CSS-5 without Fluo-4 AM at 37°C before being imaged. Live cell imaging was performed with a Zeiss epifluorescence microscope using a 40× oil-immersion objective with images being taken every 2 s. Following 3 min of baseline measurements (F_0), cells were stimulated with 50 or 100 μM of

glutamate (F). Fluorescence intensities were then quantified in individual cells using the software VisiView® (Visitron Systems). Data are represented as ΔF ($F–F_0$) normalized to baseline measurements (F_0).

In-vitro 5-ethynyl-2′-deoxyuridine (EdU) assay

To assess proliferation of eNPCs and smNPCs, cells were seeded on glass coverslips coated with laminin or Matrigel, respectively. On the next day, 5-ethynyl-2′-deoxyuridine (EdU, dissolved in PBS), at a final concentration of 10 μM, was directly added to the medium. Cells were placed back into the incubator for 1 h, then fixed with 4% PFA and washed in PBS. EdU$^+$ cells were detected using the EdU Click-iT kit (Life Technologies), followed by Hoechst-33342 counterstaining. Per condition, images from 10 to 15 fields were taken on a LSM700 confocal microscope (Zeiss) with a 20× objective. The total cell number (based on Hoechst-33342 staining) as well as the number of EdU$^+$ cells was then automatically quantified in CellProfiler (McQuin et al, 2018).

In-vivo 5-ethynyl-2′-deoxyuridine (EdU) experiments

For cortical neurogenesis experiments at P3, pregnant females received one i.p. injection of EdU (100 mg/kg, dissolved in saline; Sigma) at E14.5–15.5 and pups were then sacrificed 3 days after birth. EdU$^+$ cells were detected using the Click-iT EdU kit (Life Technologies) according to the manufacturer's instructions. Images of the entire brain were then acquired with an epifluorescence microscope using a 20× objective. EdU$^+$ cells as well as EdU$^+$ NeuN$^-$ and EdU$^+$ S100β$^+$ cells were manually quantified within the cortex of three consecutive sections.

For aNPC proliferation experiments, 4 to 5 month-old animals received three intraperitoneal (i.p.) injections of EdU (100 mg/kg, dissolved in saline; Sigma) with an inter-injection interval of 4 h. After 24 h from the last injection, animals were sacrificed via transcardial perfusion with 4% PFA. EdU$^+$ cells were detected using the Click-iT EdU kit (Life Technologies) according to the manufacturer's instructions. Images (z-stacks with 10 optical sections, 1.5 μm between planes) were acquired on a LSM700 confocal microscope with a 20× objective. Following maximum intensity projection, EdU$^+$ cells were manually quantified within the dentate gyrus (DG) of three consecutive serial sections using ZEN blue (Zeiss). Imaging and image analysis were done by an experimenter blinded to mouse genotypes. For aNPC differentiation experiments, 3-month- old mice received i.p. injections of EdU (100 mg/kg, dissolved in saline) twice daily (8 h apart) for three consecutive days. Animals were then sacrificed through transcardial perfusion 21 days after the last injection. EdU$^+$ cells were detected using the Click-iT EdU kit, followed by regular immunohistochemistry for DCX and S100β to label immature neurons and astrocytes, respectively. Images (z-stacks with 10 optical sections, 1.5 μm between planes) were acquired on a LSM900 confocal microscope with a 20× objective. Following maximum intensity projection, EdU$^+$ cells as well as EdU$^+$ DCX$^+$ and EdU$^+$ S100β$^+$ cells were manually quantified in the DG of three consecutive serial sections using ZEN blue (Zeiss). Imaging and image analysis were done by an experimenter informed about mouse genotypes.

Nuclear extraction

Cells were scraped in PBS on ice, pelleted (2,000 g, 3 min, 4°C) and incubated in hypotonic buffer (10 mM of Tris–HCl pH 7.5, 10 mM of KCl, 1.5 mM of $MgCl_2$, 1 mM of DTT, 1 mM of PMSF) for 10 min on ice. After vortexing and centrifugation (9,000 g, 10 min, 4°C), nuclear pellets were resuspended in high-salt buffer (50 mM of Tris–HCl, 300 mM of KCl, 1 mM of $MgCl_2$, 1 mM of EDTA, 1% NP-40, 1 mM of DTT, 1 mM of PMSF) and incubated for 1 h at 4°C on a rotator. The chromatin fraction was then pellet by centrifugation (20,000 g, 30 min, 4°C) and the supernatant used for co-IP or density sedimentation experiments.

Oxygen consumption rate measurements

For oxygen consumption rate (OCR) measurements in eNPCs and smNPCs, cells were seeded on cell culture microplates (Agilent Seahorse XF24) in culture media (supplemented with 3 μM of CHIR99021 or DMSO where indicated) 24 h (proliferating NPCs) to 72 h (differentiated eNPCs) before the assay. For OCR measurements in iPSCs, dissociated iPSC colonies were seeded onto cell culture microplates in culture medium (StemMACS™ iPS-Brew, Miltenyi Biotec) supplemented with 1 μM of ROCK inhibitor (Y-27632, Miltenyi Biotec, Germany) 48 h before the assay. Fresh medium without ROCK inhibitor was added on the next day and cells were cultured for an additional 24 h. On the day of the experiment, growth media were replaced with Seahorse XF base medium (Agilent), supplemented with 1 mM of pyruvate, 10 mM of glucose, and 2 mM of glutamine. Cells were then equilibrated for 60 min in a CO_2-free incubator at 37°C. Thereafter, cells were placed into a Seahorse XFe24 Analyzer (Agilent), and, after three baseline measurements, oligomycin, carbonyl cyanide-*p*-trifluoromethoxyphenylhydrazone (FCCP), and rotenone/antimycin A were successively added to profile mitochondrial respiration. The following final concentrations of compounds were used: for eNPCs: 0.5 μM of oligomycin, 2 μM of FCCP, 0.5 μM of rotenone/antimycin A; for smNPCs: 1 μM of oligomycin, 1 μM of FCCP, 0.5 μM of rotenone/antimycin A; for iPSCs: 0.5 μM of oligomycin, 1 μM of FCCP, 0.5 μM of rotenone/antimycin A. At the end of OCR assessments, cells were collected, lysed, and sonicated in RIPA buffer. Protein concentrations were then determined via Bradford assay (Sigma) and raw OCR values normalized to the respective protein content.

Proximity ligation assay

Proximity ligation assay (PLA) was done using the Duolink *In-Situ* Detection Kit (Sigma) according to the manufacturer's instructions and as published previously (Bertan *et al*, 2021). Briefly, brain sections were washed in PBS and heat-mediated antigen retrieval was performed in citrate buffer (pH 6.0). Following three washing steps, sections were permeabilized in 0.5% Trinton X-100 in PBS for 30 min at room temperature, washed again in PBS, and then incubated in blocking solution for 1 h at 37°C. Samples were then incubated with primary antibodies (NDUFB8 and MTCO1) in antibody diluent for 48–72 h at 4°C with constant agitation. After three washes in wash buffer A, sections were incubated with PLA probes in antibody diluent for 24 h at 4°C. Samples were washed again with wash buffer A and then subjected to ligation reactions via incubation in Ligation-Ligase solution (diluted in ultrapure H_2O) for 1 h

at 37°C. Amplification reaction was performed after two washes in wash buffer A by incubation in Amplification-Polymerase solution (diluted in ultrapure H_2O) for 2 h at 37°C. After two washes in wash buffer B, sections were incubated with primary antibodies (NeuN and TOM20) overnight at 4°C followed by regular immunohistochemistry procedure as described above. Samples were kept in the dark at 4°C and imaged within 48 h.

Imaging was done on a LSM800 confocal microscope with Airyscan detector (Zeiss) using a 63× oil-immersion objective. PLA measurements were obtained from z-stacks of 8–10 images at a thickness of 0.5 μm between focal planes. Images were Airyscan-processed in ZEN blue (Zeiss) and maximum intensity projections were done in ImageJ which was also used for the quantitative analysis of PLA dots. First, a mitochondrial mask was generated based on the staining of the mitochondrial marker TOM20 to measure the mitochondrial area. PLA dots were then counted within this mask using the ImageJ "find maxima" function and the total number of PLA dots was normalized to the respective mitochondrial area. Per mouse, 3–4 z-stacks from different hippocampal brain sections were imaged and analyzed.

RNA extraction and RT-PCR

RNA was extracted from cell pellets or snap-frozen tissue samples using an RNA extraction kit (QIAGEN) according to the manufacturer's instructions. Approximately 100–200 ng of isolated mRNA was retro-transcribed with qScript cDNA SuperMix (Quanta Biosciences) and reactions were carried out using Fast SYBR Green Master Mix on a StepOne Plus Thermocycler (Applied Biosystems). The following primers were used:

Bcl7a	Fw GAGAAGAAATGGGTGACCGT
	Rev TCGTCCTTGCCTTTCTTCTTG
Bcl7b	Fw GGGAGAAGAAATGGGTGACTG
	Rev TCCTTGCTATCTGTCACAGGC.
TUBB3	Fw CCTCCGTGTAGTGACCCTT
	Rev GGCCTTTGGACATCTCTTCAG
GFAP	Fw AGGTCCATGTGGAGCTTGAC
	Rev GCCATTGCCTCATACTGCGT
NANOG	Fw ACAACTGGCCGAAGAATAGCA
	Rev GGTTCCCAGTCGGGTTCAC
OCT4	Fw GACAGGGGGAGGGGAGGAGCTAGG
	Rev CTTCCCTCCAACCAGTTGCCCCAAAC
FGF4	Fw CTCTATGGCTCGCCCTTCT
	Rev GAACATGCCGGGGTACTTGT
FOS	Fw GCCTCTCTTACTACCACTCACC
	Rev AGATGGCAGTGACCGTGGGAAT

RNA sequencing

At the indicated time points, cells were scraped, collected, and pelleted in PBS. Cell pellets of approximately 500,000 cells were then lysed in Trizol, snap-frozen, and stored at −80°C until use RNA was quantified via HS RNA assay on a Tapestation4200

instrument (Agilent). Approximately 100 ng of extracted ribosome-bound RNA were used as an input for RNA-Seq library preparation according to the TruSeq Stranded mRNA kit (Illumina) following manufacturer's instructions. NGS libraries were quantified via Qubit HS dsDNA assay (Invitrogen) and library size distribution was determined using a HS D1000 assay on a Tapestation4200 instrument (Agilent). Libraries were equimolarly pooled, clustered at 1.8 pM concentration, and sequenced SR 75 cycles using High Output v2 chemistry on a NextSeq500 instrument (Illumina). Samples were demultiplexed and base call files were converted into Fastq format using bcl2fastq2 v2.20 software (Illumina) before alignment to the mouse genome mm10 build GRCm38 using STAR aligner. Data are available at GSE210760, whereas statistical analysis of differentially expressed genes can be found in Dataset EV1. Data analysis was performed using Shiny-Seq (Sundararajan et al, 2019). Gene and pathway enrichment analysis was performed using an online gene ontology software (www.geneontology.org) and Ingenuity Pathway Analysis (IPA, Qiagen).

Statistics

Data are represented as mean ± SEM and were statistically analyzed using Graph Pad Prism. For normally distributed data, Student's t test, one- or two-way ANOVA with repeated measures where appropriate, followed by Bonferroni's or Tukey's t-test was performed. In case of nonnormally distributed data, Mann–Whitney or Kruskal–Wallis test was used. The number of biological replicates/independent experiments is stated in the Figure legends. Levels of significance are indicated as $*P < 0.05$, $**P < 0.01$, $***P < 0.001$, $****P < 0.0001$.

Transgenic mice

Mice were kept in cages of two to four with free access to food (ssniff® V1534-300) and tap water under a 12 h/12 h light/dark cycle (lights on at 6:00 am). $Bcl7a^{fl/fl}$ and $Bcl7b^{fl/fl}$ mice were generated by inGenious Targeting Laboratory as described previously (Wischhof et al, 2017). For the generation of $Bcl7a$ and $Bcl7b$ full knockout mice, $Bcl7a^{fl/fl}$ and $Bcl7b^{fl/fl}$ males were first crossed with females carrying a CMV-transgene and heterozygous animals were then used for subsequent crosses to generate $Bcl7a$ and $Bcl7b$ full knockout mice. Conditional $Bcl7a$ knockout mice were generated via crossed of $Bcl7a^{fl/fl}$ males with females carrying the $Nestin$- or $Baf53b$-Cre transgene. CMV-, Nestin-, and BAF53B-Cre deleter lines were purchased from the Jackson Laboratory (JAX stock numbers: CMV-$Cre^{tg/wt}$: 006054, $Nestin$-$Cre^{tg/wt}$: 003771, $Baf53b$-$Cre^{tg/wt}$: 027826). All mouse lines were kept on a C57BL/6 background. Experiments were performed with equal numbers of male and female mice. All experimental procedures were performed in accordance with the institutional animal welfare guideline and were approved by the State Agency for Nature, Environment and Consumer Protection (LANUV) of North Rhine Westphalia (Germany; animal licenses: 81-02.04.2018.A121, 81.02.04.2018.A224, 81-02.04.2020.A110).

Western blotting

Western blot analysis was performed using standard procedures. Cell pellets and snap-frozen tissue samples were lysed and sonicated in ice-cold RIPA buffer (Sigma) supplemented with protease and phosphatase inhibitors (Roche). Proteins were separated on 7–15% SDS-PAGE gels, according to their molecular weight, and transferred onto nitrocellulose membranes (Bio-Rad). Membranes were blocked in 5% milk or BSA in TBST and incubated with primary antibodies overnight at 4°C. Thereafter, membranes were washed in TBST and incubated with appropriate HRP-conjugated secondary antibodies for 1 h at room temperature. Following three washing steps, immunoblots were imaged using a ChemiDoc Imager (Bio-Rad). For densitometries, band intensities were quantified with ImageJ.

Data availability

The ChIP-seq and the RNA-seq data have been deposited to NCBI GEO database under the common accession number GSE210760: https://www.ncbi.nlm.nih.gov/geo/query/acc.cgi?acc = GSE210760

Expanded View for this article is available online.

Author contributions

Lena Wischhof: Conceptualization; formal analysis; supervision; validation; investigation; visualization; methodology; writing – original draft; writing – review and editing. **Hang-Mao Lee:** Formal analysis; visualization. **Janine Tutas:** Investigation. **Clemens Overkott:** Investigation. **Eileen Tedt:** Investigation. **Miriam Stork:** Resources. **Michael Peitz:** Resources. **Oliver Brüstle:** Resources. **Thomas Ulas:** Formal analysis. **Kristian Händler:** Formal analysis. **Joachim L Schultze:** Resources. **Dan Ehninger:** Resources. **Pierluigi Nicotera:** Funding acquisition. **Paolo Salomoni:** Formal analysis; writing – original draft. **Daniele Bano:** Conceptualization; formal analysis; supervision; funding acquisition; visualization; writing – original draft; project administration; writing – review and editing.

Disclosure and competing interests statement

The authors declare that they have no conflict of interest.

References

Adusumilli VS, Walker TL, Overall RW, Klatt GM, Zeidan SA, Zocher S, Kirova DG, Ntitsias K, Fischer TJ, Sykes AM *et al* (2021) ROS dynamics delineate functional states of hippocampal neural stem cells and link to their activity-dependent exit from quiescence. *Cell Stem Cell* 28: 300–314

Aguirre A, Rubio ME, Gallo V (2010) Notch and EGFR pathway interaction regulates neural stem cell number and self-renewal. *Nature* 467: 323–327

Alajem A, Biran A, Harikumar A, Sailaja BS, Aaronson Y, Livyatan I, Nissim-Rafinia M, Sommer AG, Mostoslavsky G, Gerbasi VR *et al* (2015) Differential association of chromatin proteins identifies BAF60a/SMARCD1 as a regulator of embryonic stem cell differentiation. *Cell Rep* 10: 2019–2031

Alfert A, Moreno N, Kerl K (2019) The BAF complex in development and disease. *Epigenetics Chromatin* 12: 19

Bachmann C, Nguyen H, Rosenbusch J, Pham L, Rabe T, Patwa M, Sokpor G, Seong RH, Ashery-Padan R, Mansouri A *et al* (2016) mSWI/SNF (BAF) complexes are indispensable for the neurogenesis and development of embryonic olfactory epithelium. *PLoS Genet* 12: e1006274

Balinas-Gavira C, Rodriguez MI, Andrades A, Cuadros M, Alvarez-Perez JC, Alvarez-Prado AF, de Yebenes VG, Sanchez-Hernandez S, Fernandez-Vigo E, Munoz J *et al* (2020) Frequent mutations in the amino-terminal domain of BCL7A impair its tumor suppressor role in DLBCL. *Leukemia* 34: 2722–2735

Bano D, Dinsdale D, Cabrera-Socorro A, Maida S, Lambacher N, McColl B, Ferrando-May E, Hengartner MO, Nicotera P (2010) Alteration of the nuclear pore complex in Ca(2+)-mediated cell death. *Cell Death Differ* 17: 119–133

Barker N, Hurlstone A, Musisi H, Miles A, Bienz M, Clevers H (2001) The chromatin remodelling factor Brg-1 interacts with beta-catenin to promote target gene activation. *EMBO J* 20: 4935–4943

Beckervordersandforth R, Ebert B, Schaffner I, Moss J, Fiebig C, Shin J, Moore DL, Ghosh L, Trinchero MF, Stockburger C *et al* (2017) Role of mitochondrial metabolism in the control of early lineage progression and aging phenotypes in adult hippocampal neurogenesis. *Neuron* 93: e566

Bertan F, Wischhof L, Scifo E, Guranda M, Jackson J, Marsal-Cots A, Piazzesi A, Stork M, Peitz M, Prehn JHM *et al* (2021) Comparative analysis of CI- and CIV-containing respiratory supercomplexes at single-cell resolution. *Cell Rep Methods* 1: 100002

Bindea G, Mlecnik B, Hackl H, Charoentong P, Tosolini M, Kirilovsky A, Fridman WH, Pages F, Trajanoski Z, Galon J (2009) ClueGO: a Cytoscape plug-in to decipher functionally grouped gene ontology and pathway annotation networks. *Bioinformatics* 25: 1091–1093

Bogacka I, Xie H, Bray GA, Smith SR (2005) Pioglitazone induces mitochondrial biogenesis in human subcutaneous adipose tissue in vivo. *Diabetes* 54: 1392–1399

Bond AM, Ming GL, Song H (2015) Adult mammalian neural stem cells and neurogenesis: five decades later. *Cell Stem Cell* 17: 385–395

Bracken AP, Brien GL, Verrijzer CP (2019) Dangerous liaisons: interplay between SWI/SNF, NuRD, and Polycomb in chromatin regulation and cancer. *Genes Dev* 33: 936–959

Choi KY, Yoo M, Han JH (2015) Toward understanding the role of the neuron-specific BAF chromatin remodeling complex in memory formation. *Exp Mol Med* 47: e155

Ciruna B, Jenny A, Lee D, Mlodzik M, Schier AF (2006) Planar cell polarity signalling couples cell division and morphogenesis during neurulation. *Nature* 439: 220–224

Conboy IM, Conboy MJ, Wagers AJ, Girma ER, Weissman IL, Rando TA (2005) Rejuvenation of aged progenitor cells by exposure to a young systemic environment. *Nature* 433: 760–764

Costa R, Peruzzo R, Bachmann M, Monta GD, Vicario M, Santinon G, Mattarei A, Moro E, Quintana-Cabrera R, Scorrano L *et al* (2019) Impaired mitochondrial ATP production downregulates Wnt signaling via ER stress induction. *Cell Rep* 28: 1949–1960

Dragunow M, Faull R (1989) The use of c-fos as a metabolic marker in neuronal pathway tracing. *J Neurosci Methods* 29: 261–265

Erickson KI, Voss MW, Prakash RS, Basak C, Szabo A, Chaddock L, Kim JS, Heo S, Alves H, White SM *et al* (2011) Exercise training increases size of hippocampus and improves memory. *Proc Natl Acad Sci USA* 108: 3017–3022

Falk S, Gotz M (2017) Glial control of neurogenesis. *Curr Opin Neurobiol* 47: 188–195

Geling A, Steiner H, Willem M, Bally-Cuif L, Haass C (2002) A gamma-secretase inhibitor blocks notch signaling in vivo and causes a severe neurogenic phenotype in zebrafish. *EMBO Rep* 3: 688–694

Goncalves JT, Schafer ST, Gage FH (2016) Adult neurogenesis in the hippocampus: from stem cells to behavior. *Cell* 167: 897–914

Gotz M, Nakafuku M, Petrik D (2016) Neurogenesis in the developing and adult brain-similarities and key differences. *Cold Spring Harb Perspect Biol* 8: a018853

Haussmann IU, White K, Soller M (2008) Erect wing regulates synaptic growth in drosophila by integration of multiple signaling pathways. *Genome Biol* 9: R73

Helming KC, Wang X, Roberts CW (2014) Vulnerabilities of mutant SWI/SNF complexes in cancer. *Cancer Cell* 26: 309–317

Heppt J, Wittmann MT, Schaffner I, Billmann C, Zhang J, Vogt-Weisenhorn D, Prakash N, Wurst W, Taketo MM, Lie DC (2020) Beta-catenin signaling modulates the tempo of dendritic growth of adult-born hippocampal neurons. *EMBO J* 39: e104472

Hohmann AF, Vakoc CR (2014) A rationale to target the SWI/SNF complex for cancer therapy. *Trends Genet* 30: 356–363

Imayoshi I, Sakamoto M, Yamaguchi M, Mori K, Kageyama R (2010) Essential roles of notch signaling in maintenance of neural stem cells in developing and adult brains. *J Neurosci* 30: 3489–3498

Inak G, Rybak-Wolf A, Lisowski P, Pentimalli TM, Juttner R, Glazar P, Uppal K, Bottani E, Brunetti D, Secker C *et al* (2021) Defective metabolic programming impairs early neuronal morphogenesis in neural cultures and an organoid model of Leigh syndrome. *Nat Commun* 12: 1929

Iram T, Kern F, Kaur A, Myneni S, Morningstar AR, Shin H, Garcia MA, Yerra L, Palovics R, Yang AC *et al* (2022) Young CSF restores oligodendrogenesis and memory in aged mice via Fgf17. *Nature* 605: 509–515

Kadoch C, Copeland RA, Keilhack H (2016) PRC2 and SWI/SNF chromatin remodeling complexes in health and disease. *Biochemistry* 55: 1600–1614

Kadoch C, Crabtree GR (2015) Mammalian SWI/SNF chromatin remodeling complexes and cancer: Mechanistic insights gained from human genomics. *Sci Adv* 1: e1500447

Kadoch C, Hargreaves DC, Hodges C, Elias L, Ho L, Ranish J, Crabtree GR (2013) Proteomic and bioinformatic analysis of mammalian SWI/SNF complexes identifies extensive roles in human malignancy. *Nat Genet* 45: 592–601

Kadoch C, Williams RT, Calarco JP, Miller EL, Weber CM, Braun SM, Pulice JL, Chory EJ, Crabtree GR (2017) Dynamics of BAF-Polycomb complex opposition on heterochromatin in normal and oncogenic states. *Nat Genet* 49: 213–222

Kaeser MD, Aslanian A, Dong MQ, Yates JR III, Emerson BM (2008) BRD7, a novel PBAF-specific SWI/SNF subunit, is required for target gene activation and repression in embryonic stem cells. *J Biol Chem* 283: 32254–32263

Kalani MY, Cheshier SH, Cord BJ, Bababeygy SR, Vogel H, Weissman IL, Palmer TD, Nusse R (2008) Wnt-mediated self-renewal of neural stem/progenitor cells. *Proc Natl Acad Sci USA* 105: 16970–16975

Kempermann G (2015) Activity dependency and aging in the regulation of adult neurogenesis. *Cold Spring Harb Perspect Biol* 7: a018929

Kempermann G, Gage FH, Aigner L, Song H, Curtis MA, Thuret S, Kuhn HG, Jessberger S, Frankland PW, Cameron HA *et al* (2018) Human adult neurogenesis: evidence and remaining questions. *Cell Stem Cell* 23: 25–30

Kempermann G, Song H, Gage FH (2015) Neurogenesis in the adult hippocampus. *Cold Spring Harb Perspect Biol* 7: a018812

Khacho M, Clark A, Svoboda DS, Azzi J, MacLaurin JG, Meghaizel C, Sesaki H, Lagace DC, Germain M, Harper ME *et al* (2016) Mitochondrial dynamics impacts stem cell identity and fate decisions by regulating a nuclear transcriptional program. *Cell Stem Cell* 19: 232–247

Kim KH, Kim W, Howard TP, Vazquez F, Tsherniak A, Wu JN, Wang W, Haswell JR, Walensky LD, Hahn WC *et al* (2015) SWI/SNF-mutant cancers depend on catalytic and non-catalytic activity of EZH2. *Nat Med* 21: 1491–1496

Langmead B, Salzberg SL (2012) Fast gapped-read alignment with bowtie 2. *Nat Methods* 9: 357–359

Lessard J, Wu JI, Ranish JA, Wan M, Winslow MM, Staahl BT, Wu H, Aebersold R, Graef IA, Crabtree GR (2007) An essential switch in subunit composition of a chromatin remodeling complex during neural development. *Neuron* 55: 201–215

Liang H, Hippenmeyer S, Ghashghaei HT (2012) A nestin-cre transgenic mouse is insufficient for recombination in early embryonic neural progenitors. *Biol Open* 1: 1200–1203

Lie DC, Colamarino SA, Song HJ, Desire L, Mira H, Consiglio A, Lein ES, Jessberger S, Lansford H, Dearie AR *et al* (2005) Wnt signalling regulates adult hippocampal neurogenesis. *Nature* 437: 1370–1375

Lim DA, Alvarez-Buylla A (2016) The adult ventricular-subventricular zone (V-SVZ) and olfactory bulb (OB) neurogenesis. *Cold Spring Harb Perspect Biol* 8: a018820

Lorenz C, Lesimple P, Bukowiecki R, Zink A, Inak G, Mlody B, Singh M, Semtner M, Mah N, Aure K *et al* (2017) Human iPSC-derived neural progenitors are an effective drug discovery model for neurological mtDNA disorders. *Cell Stem Cell* 20: 659–674

Ma Z, Wang H, Cai Y, Wang H, Niu K, Wu X, Ma H, Yang Y, Tong W, Liu F *et al* (2018) Epigenetic drift of H3K27me3 in aging links glycolysis to healthy longevity in *Drosophila*. *Elife* 7: e35368

Madabhushi R, Gao F, Pfenning AR, Pan L, Yamakawa S, Seo J, Rueda R, Phan TX, Yamakawa H, Pao PC *et al* (2015) Activity-induced DNA breaks govern the expression of neuronal early-response genes. *Cell* 161: 1592–1605

Mashtalir N, D'Avino AR, Michel BC, Luo J, Pan J, Otto JE, Zullow HJ, McKenzie ZM, Kubiak RL, St Pierre R *et al* (2018) Modular organization and assembly of SWI/SNF family chromatin remodeling complexes. *Cell* 175: 1272–1288

Mashtalir N, Suzuki H, Farrell DP, Sankar A, Luo J, Filipovski M, D'Avino AR, St Pierre R, Valencia AM, Onikubo T *et al* (2020) A structural model of the endogenous human BAF complex informs disease mechanisms. *Cell* 183: 802–817

McBride MJ, Pulice JL, Beird HC, Ingram DR, D'Avino AR, Shern JF, Charville GW, Hornick JL, Nakayama RT, Garcia-Rivera EM *et al* (2018) The SS18-SSX fusion oncoprotein hijacks BAF complex targeting and function to drive synovial sarcoma. *Cancer Cell* 33: 1128–1141

McQuin C, Goodman A, Chernyshev V, Kamentsky L, Cimini BA, Karhohs KW, Doan M, Ding L, Rafelski SM, Thirstrup D *et al* (2018) CellProfiler 3.0: next-generation image processing for biology. *PLoS Biol* 16: e2005970

Michel BC, D'Avino AR, Cassel SH, Mashtalir N, McKenzie ZM, McBride MJ, Valencia AM, Zhou Q, Bocker M, Soares LMM *et al* (2018) A non-canonical SWI/SNF complex is a synthetic lethal target in cancers driven by BAF complex perturbation. *Nat Cell Biol* 20: 1410–1420

Mittal P, Roberts CWM (2020) The SWI/SNF complex in cancer – biology, biomarkers and therapy. *Nat Rev Clin Oncol* 17: 435–448

Mizutani K, Yoon K, Dang L, Tokunaga A, Gaiano N (2007) Differential notch signalling distinguishes neural stem cells from intermediate progenitors. *Nature* 449: 351–355

Morgan MA, Shilatifard A (2015) Chromatin signatures of cancer. *Genes Dev* 29: 238–249

Nakayama RT, Pulice JL, Valencia AM, McBride MJ, McKenzie ZM, Gillespie MA, Ku WL, Teng M, Cui K, Williams RT *et al* (2017) SMARCB1 is required for widespread BAF complex-mediated activation of enhancers and bivalent promoters. *Nat Genet* 49: 1613–1623

Narayanan R, Pirouz M, Kerimoglu C, Pham L, Wagener RJ, Kiszka KA, Rosenbusch J, Seong RH, Kessel M, Fischer A *et al* (2015) Loss of BAF (mSWI/SNF) complexes causes global transcriptional and chromatin state changes in forebrain development. *Cell Rep* 13: 1842–1854

Obernier K, Alvarez-Buylla A (2019) Neural stem cells: origin, heterogeneity and regulation in the adult mammalian brain. *Development* 146: dev156059

Paridaen JT, Huttner WB (2014) Neurogenesis during development of the vertebrate central nervous system. *EMBO Rep* 15: 351–364

Pei Y, Brun SN, Markant SL, Lento W, Gibson P, Taketo MM, Giovannini M, Gilbertson RJ, Wechsler-Reya RJ (2012) WNT signaling increases proliferation and impairs differentiation of stem cells in the developing cerebellum. *Development* 139: 1724–1733

Puri PL, Mercola M (2012) BAF60 a, B, and Cs of muscle determination and renewal. *Genes Dev* 26: 2673–2683

Quinlan AR, Hall IM (2010) BEDTools: a flexible suite of utilities for comparing genomic features. *Bioinformatics* 26: 841–842

Ramirez F, Dundar F, Diehl S, Gruning BA, Manke T (2014) deepTools: a flexible platform for exploring deep-sequencing data. *Nucleic Acids Res* 42: W187–W191

Ramos-Medina R, Montes-Moreno S, Maestre L, Canamero M, Rodriguez-Pinilla M, Martinez-Torrecuadrada J, Piris MA, Majid A, Dyer MJ, Pulford K *et al* (2013) BCL7A protein expression in normal and malignant lymphoid tissues. *Br J Haematol* 160: 106–109

Rath S, Sharma R, Gupta R, Ast T, Chan C, Durham TJ, Goodman RP, Grabarek Z, Haas ME, Hung WHW *et al* (2021) MitoCarta3.0: an updated mitochondrial proteome now with sub-organelle localization and pathway annotations. *Nucleic Acids Res* 49: D1541–D1547

Reinhardt P, Glatza M, Hemmer K, Tsytsyura Y, Thiel CS, Hoing S, Moritz S, Parga JA, Wagner L, Bruder JM *et al* (2013) Derivation and expansion using only small molecules of human neural progenitors for neurodegenerative disease modeling. *PLoS ONE* 8: e59252

Ringrose L, Paro R (2004) Epigenetic regulation of cellular memory by the Polycomb and Trithorax group proteins. *Annu Rev Genet* 38: 413–443

Romero OA, Sanchez-Cespedes M (2014) The SWI/SNF genetic blockade: effects in cell differentiation, cancer and developmental diseases. *Oncogene* 33: 2681–2689

Ronan JL, Wu W, Crabtree GR (2013) From neural development to cognition: Unexpected roles for chromatin. *Nat Rev Genet* 14: 347–359

Russo GL, Sonsalla G, Natarajan P, Breunig CT, Bulli G, Merl-Pham J, Schmitt S, Giehrl-Schwab J, Giesert F, Jastroch M *et al* (2021) CRISPR-mediated induction of neuron-enriched mitochondrial proteins boosts direct glia-to-neuron conversion. *Cell Stem Cell* 28: e527

Sartorelli V, Puri PL (2018) Shaping gene expression by landscaping chromatin architecture: Lessons from a master. *Mol Cell* 71: 375–388

Schick S, Rendeiro AF, Runggatscher K, Ringler A, Boidol B, Hinkel M, Majek P, Vulliard L, Penz T, Parapatics K *et al* (2019) Systematic characterization of BAF mutations provides insights into intracomplex synthetic lethalities in human cancers. *Nat Genet* 51: 1399–1410

Schuettengruber B, Bourbon HM, Di Croce L, Cavalli G (2017) Genome regulation by Polycomb and Trithorax: 70 years and counting. *Cell* 171: 34–57

Shain AH, Pollack JR (2013) The spectrum of SWI/SNF mutations, ubiquitous in human cancers. *PLoS ONE* 8: e55119

Shen L, Shao NY, Liu X, Maze I, Feng J, Nestler EJ (2013) diffReps: detecting differential chromatin modification sites from ChIP-seq data with biological replicates. *PLoS ONE* 8: e65598

Sheng M, Greenberg ME (1990) The regulation and function of c-fos and other immediate early genes in the nervous system. *Neuron* 4: 477–485

Silbereis JC, Pochareddy S, Zhu Y, Li M, Sestan N (2016) The cellular and molecular landscapes of the developing human central nervous system. *Neuron* 89: 248–268

Sokpor G, Xie Y, Rosenbusch J, Tuoc T (2017) Chromatin remodeling BAF (SWI/SNF) complexes in neural development and disorders. *Front Mol Neurosci* 10: 243

Son EY, Crabtree GR (2014) The role of BAF (mSWI/SNF) complexes in mammalian neural development. *Am J Med Genet C Semin Med Genet* 166C: 333–349

Sundararajan Z, Knoll R, Hombach P, Becker M, Schultze JL, Ulas T (2019) Shiny-seq: advanced guided transcriptome analysis. *BMC Res Notes* 12: 432

Toda T, Parylak SL, Linker SB, Gage FH (2019) The role of adult hippocampal neurogenesis in brain health and disease. *Mol Psychiatry* 24: 67–87

Toto PC, Puri PL, Albini S (2016) SWI/SNF-directed stem cell lineage specification: dynamic composition regulates specific stages of skeletal myogenesis. *Cell Mol Life Sci* 73: 3887–3896

Tsurusaki Y, Okamoto N, Ohashi H, Kosho T, Imai Y, Hibi-Ko Y, Kaname T, Naritomi K, Kawame H, Wakui K *et al* (2012) Mutations affecting components of the SWI/SNF complex cause coffin-Siris syndrome. *Nat Genet* 44: 376–378

Tsurusaki Y, Okamoto N, Ohashi H, Mizuno S, Matsumoto N, Makita Y, Fukuda M, Isidor B, Perrier J, Aggarwal S *et al* (2014) Coffin-Siris syndrome is a SWI/SNF complex disorder. *Clin Genet* 85: 548–554

Tuoc T, Dere E, Radyushkin K, Pham L, Nguyen H, Tonchev AB, Sun G, Ronnenberg A, Shi Y, Staiger JF *et al* (2017) Ablation of BAF170 in developing and postnatal dentate gyrus affects neural stem cell proliferation, differentiation, and learning. *Mol Neurobiol* 54: 4618–4635

Tuoc TC, Boretius S, Sansom SN, Pitulescu ME, Frahm J, Livesey FJ, Stoykova A (2013) Chromatin regulation by BAF170 controls cerebral cortical size and thickness. *Dev Cell* 25: 256–269

Uehara T, Kage-Nakadai E, Yoshina S, Imae R, Mitani S (2015) The tumor suppressor BCL7B functions in the Wnt signaling pathway. *PLoS Genet* 11: e1004921

Valencia AM, Collings CK, Dao HT, St Pierre R, Cheng YC, Huang J, Sun ZY, Seo HS, Mashtalir N, Comstock DE *et al* (2019) Recurrent SMARCB1 mutations reveal a nucleosome acidic patch interaction site that potentiates mSWI/SNF complex chromatin remodeling. *Cell* 179: 1342–1356

Valencia AM, Kadoch C (2019) Chromatin regulatory mechanisms and therapeutic opportunities in cancer. *Nat Cell Biol* 21: 152–161

Vogel-Ciernia A, Matheos DP, Barrett RM, Kramar EA, Azzawi S, Chen Y, Magnan CN, Zeller M, Sylvain A, Haettig J *et al* (2013) The neuron-specific chromatin regulatory subunit BAF53b is necessary for synaptic plasticity and memory. *Nat Neurosci* 16: 552–561

Wang X, Lee RS, Alver BH, Haswell JR, Wang S, Mieczkowski J, Drier Y, Gillespie SM, Archer TC, Wu JN *et al* (2017) SMARCB1-mediated SWI/SNF complex function is essential for enhancer regulation. *Nat Genet* 49: 289–295

Wischhof L, Maida S, Piazzesi A, Gioran A, Barragan Sanz K, Irsen S, Beyer M, Schultze JL, Dyer MJ, Salomoni P *et al* (2017) The SWI/SNF subunit Bcl7a contributes to motor coordination and Purkinje cell function. *Sci Rep* 7: 17055

Wu JI, Lessard J, Olave IA, Qiu Z, Ghosh A, Graef IA, Crabtree GR (2007) Regulation of dendritic development by neuron-specific chromatin remodeling complexes. *Neuron* 56: 94–108

Yao B, Christian KM, He C, Jin P, Ming GL, Song H (2016) Epigenetic mechanisms in neurogenesis. *Nat Rev Neurosci* 17: 537–549

Yoo M, Choi KY, Kim J, Kim M, Shim J, Choi JH, Cho HY, Oh JP, Kim HS, Kaang BK *et al* (2017) BAF53b, a neuron-specific nucleosome remodeling factor, is induced after learning and facilitates long-term memory consolidation. *J Neurosci* 37: 3686–3697

Yoon JC, Ng A, Kim BH, Bianco A, Xavier RJ, Elledge SJ (2010) Wnt signaling regulates mitochondrial physiology and insulin sensitivity. *Genes Dev* 24: 1507–1518

Zani VJ, Asou N, Jadayel D, Heward JM, Shipley J, Nacheva E, Takasuki K, Catovsky D, Dyer MJ (1996) Molecular cloning of complex chromosomal translocation t(8;14;12)(q24.1;q32.3;q24.1) in a Burkitt lymphoma cell line defines a new gene (BCL7A) with homology to caldesmon. *Blood* 87: 3124–3134

Zechner D, Fujita Y, Hulsken J, Muller T, Walther I, Taketo MM, Crenshaw EB III, Birchmeier W, Birchmeier C (2003) Beta-catenin signals regulate cell growth and the balance between progenitor cell expansion and differentiation in the nervous system. *Dev Biol* 258: 406–418

Zhan X, Cao M, Yoo AS, Zhang Z, Chen L, Crabtree GR, Wu JI (2015) Generation of BAF53b-Cre transgenic mice with pan-neuronal Cre activities. *Genesis* 53: 440–448

Zhang T, Cooper S, Brockdorff N (2015) The interplay of histone modifications - writers that read. *EMBO Rep* 16: 1467–1481

Zhu B, Ueda A, Song X, Horike SI, Yokota T, Akagi T (2017) Baf53a is involved in survival of mouse ES cells, which can be compensated by Baf53b. *Sci Rep* 7: 14059

Ziviani E, Lippi G, Bano D, Munarriz E, Guiducci S, Zoli M, Young KW, Nicotera P (2011) Ryanodine receptor-2 upregulation and nicotine-mediated plasticity. *EMBO J* 30: 194–204